



# Oligodendroglia vulnerability in the human dorsal striatum in Parkinson's disease

Juan M. Barba-Reyes<sup>1</sup> · Lisbeth Harder<sup>2</sup> · Sergio Marco Salas<sup>3,4</sup> · Methasit Jaisa-aad<sup>5,6</sup> · Clara Muñoz-Castro<sup>5,6</sup> · Leonardo D. Garma<sup>2</sup> · Nima Rafati<sup>7</sup> · Mats Nilsson<sup>3</sup> · Bradley T. Hyman<sup>5,6</sup> · Alberto Serrano-Pozo<sup>5,6</sup> · Ana B. Muñoz-Manchado<sup>1,2,8</sup>

Received: 13 February 2025 / Revised: 15 April 2025 / Accepted: 23 April 2025  
© The Author(s) 2025

## Abstract

Oligodendroglia are the responsible cells for myelination in the central nervous system and their involvement in Parkinson's disease (PD) is poorly understood. We performed sn-RNA-seq and image-based spatial transcriptomics of human caudate nucleus and putamen (dorsal striatum) from PD and control brain donors to elucidate the diversity of oligodendroglia and how they are affected by the disease. We profiled a total of ~200,000 oligodendroglial nuclei, defining 15 subclasses, from precursor to mature cells, 4 of which are disease-associated. These PD-specific populations are characterized by the overexpression of heat shock proteins, as well as distinct expression signatures related to immune responses, myelination alterations, and disrupted cell signaling pathways. We have also identified impairments in cell communication and oligodendrocyte development, evidenced by changes in neurotransmitter receptors expression and cell adhesion molecules. In addition, we observed significant disruptions in oligodendrocyte development, with aberrant differentiation trajectories and shifts in cell proportions, particularly in the transition from mature oligodendrocytes to disease-associated states. Quantitative immunohistochemical analysis revealed decreased myelin levels in the PD striatum, which correlated with transcriptomic alterations. Furthermore, spatial transcriptomics mapping revealed the distinct localization of disease-associated populations within the striatum, with evidence of impaired myelin integrity. Thus, we uncover oligodendroglia as a critical cell type in PD and a potential new therapeutic target for myelin-based interventions.

**Keywords** Neurodegeneration · Sc-RNA-seq · Spatial transcriptomics · Striatum · Oligodendrocyte · Myelin

## Abbreviations

PD	Parkinson's disease	sc/sn-RNA-seq	Single-cell/single-nucleus RNA sequencing
SNpc	Substantia nigra pars compacta	OPCs	Oligodendrocyte progenitor cells
LBs	Lewy bodies	MS	Multiple sclerosis
LN <sub>s</sub>	Lewy neurites	GWAS	Genome Wide Association Studies
OL <sub>s</sub>	Oligodendrocytes	Pu	Putamen
AD	Alzheimer's disease	CN	Caudate nucleus
		PDA-OL <sub>s</sub>	PD-associated oligodendrocytes

✉ Ana B. Muñoz-Manchado  
ana.munoz@uca.es

<sup>1</sup> Unit of Cell Biology, Department of Neuroscience, Institute for Biomedical Research and Innovation of Cádiz (INiBICA), University of Cádiz, Cádiz, Spain

<sup>2</sup> Laboratory of Molecular Neurobiology, Department of Medical Biochemistry and Biophysics, Karolinska Institutet, Stockholm, Sweden

<sup>3</sup> Science for Life Laboratory, Department of Biochemistry and Biophysics, Stockholm University, Stockholm, Sweden

<sup>4</sup> Institute of Computational Biology, Computational Health Center, Helmholtz, Munich, Germany

<sup>5</sup> Department of Neurology, Massachusetts General Hospital, Boston, MA, USA

<sup>6</sup> Harvard Medical School, Boston, MA, USA

<sup>7</sup> National Bioinformatics Infrastructure Sweden, Science for Life Laboratory, Department of Medical Biochemistry and Microbiology, Uppsala University, Uppsala, Sweden

<sup>8</sup> Ciber of Mental Health (CIBERSAM), ISCIII, 28029 Madrid, Spain

FACS	Fluorescent-activated cell sorting
RT	Reverse transcription
UMIs	Unique molecular identifiers
PCA	Principal component analysis
PCs	Principal components
scCODA	Single-cell compositional data analysis
GSEA	Gene Set Enrichment Analysis
NES	Normalized Enrichment Score
FDR	False discovery rate
GO	Gene ontology
KEGG	Kyoto Encyclopedia of Genes and Genomes
MBP	Myelin basic protein
TH	Tyrosine hydroxylase
ROIs	Regions of interest
$\alpha$ -syn	$\alpha$ -Synuclein
kNN	K-nearest neighbors
GCN	Graph convolutional network
WM	White matter
GM	Gray matter
SEM	Standard error mean
COPs	Committed OPCs
MOL	Mature oligodendrocytes
HSP	Heat shock proteins
immOL	Immature OLs
TCA	Citric acid
LAMA2	Laminin-2
ECM	Extracellular matrix
CAMs	Cell adhesion molecules
HSPR	Heat shock protein response
MSA	Multiple system atrophy

## Introduction

Parkinson's disease (PD) has a significant impact on society due to its widespread implications both in patients' health and caretakers, with a rapid increase in incidence over the past 2 decades [55, 57]. PD is a heterogeneous condition, with mutations in multiple genes presenting with a similar parkinsonian syndrome and a single causative mutation resulting in a range of clinical presentations [9, 36]. This heterogeneity suggests different underlying mechanisms at a biological level that are not yet fully understood. While the loss of dopaminergic neurons in the *substantia nigra pars compacta* (SNpc) and the accumulation of intracellular  $\alpha$ -synuclein aggregates in Lewy bodies (LBs) and Lewy neurites (LNs) have long been associated with the development of PD [21, 31], recent studies have demonstrated the involvement of glial cells, in particular oligodendrocytes (OLs), in neurodegenerative disorders such as PD and Alzheimer's disease (AD) [16, 23, 29, 47, 48, 52, 62, 64, 85].

While they have traditionally been considered homogeneous populations [4, 15, 34], recent advancements including single-cell/single-nucleus RNA sequencing (sc/sn-RNA-seq) have revealed that OLs are heterogeneous, comprising numerous subpopulations and states that participate in distinct biological processes [35, 46], redefining the maturation process as a continuum. Indeed, OLs are known to progress through distinct developmental states, starting as oligodendrocyte progenitor cells (OPCs), which proliferate and differentiate into pre-myelinating OLs, that eventually mature into fully myelinating oligodendrocytes [5, 12]. These different states correspond to distinct transcriptomic and morphologic profiles that can also vary along brain regions [6, 7, 40, 65, 75, 77].

Recent works suggest that alterations in myelin integrity and OL survival can play a crucial role in the progression of neurodegenerative diseases and MS [30, 35, 46–48, 62]. Interestingly a few studies have also demonstrated a connection between OLs and PD [2, 3, 13, 51, 79]. Bryois et al. [13] found a genetic association between PD GWAS variants and OLs, while Wakabayashi et al. [79] and Arai et al. [2] observed  $\alpha$ -synuclein inclusions in OLs of PD brains. These findings suggest that OLs may play a critical role in the development of PD. However, few studies have investigated the role of the OL lineage in PD, particularly in the dorsal striatum [3, 72], a brain region that includes the putamen (Pu) and caudate nucleus (CN) and is central to PD pathophysiology [41] and therapeutic development, as it receives the nigrostriatal axons from the dopaminergic neurons of the SNpc [71].

In this study, we elucidated the transcriptomic changes induced by PD across OLs lineage populations using sn-RNA-seq in the dorsal striatum from 63 donors and image-based spatial transcriptomics in a subset of them. Our results reveal distinct transcriptomic states of PD-associated oligodendrocytes (PDA-OLs), delineating diverse altered functional pathways, the spatial organization of OLs, and the potential biological consequences of OL dysfunction for the extent of both dopaminergic neuron loss and LB/LN formation.

## Materials and methods

### Human tissue

Human brain samples for this study were obtained from donors with a clinical and neuropathological diagnosis of PD and controls not meeting clinical or neuropathological diagnostic criteria for any neurodegenerative disease. Specifically, the CN and Pu were dissected from coronal slabs at the level of the *nucleus accumbens*. The control group comprised 27 individuals (Pu = 27, CN = 24)

ranging in age from 25 to over 90 years. The PD group included 36 individuals (Pu = 35, CN = 34) aged between 60 and over 90 years. Samples were collected from three sources: the Human Brain and Spinal Fluid Resource Center (Los Angeles, CA, USA), the Parkinson's UK Brain Bank at Imperial College London (London, UK), and the Massachusetts Alzheimer's Disease Research Center (Charlestown, MA, USA). Donors or their next-of-kin provided written informed consent for brain autopsy, and the study was approved by the review board of each brain bank. Detailed information regarding the samples is provided in Supplementary Table 1. Since PD is more common in men, the control and PD groups were not matched by sex (i.e., there were 19 females and 44 males in the full cohort, control: 18/9 and PD: 26/10 male/female). Consequently, the study lacks sufficient power to robustly analyze sex-specific effects, such as differences in cell class proportions or the influence of sex on gene expression regulation.

### Tissue dissociation

Nuclei isolation from fresh frozen tissue was conducted following the protocol outlined by the Allen Institute for Brain Science (<https://www.protocols.io/view/isolation-of-nuclei-from-adult-human-brain-tissue-eq2lyd1nqlx9/v2>), with specific guidelines. All procedures were performed at 4 °C to maintain sample integrity. Tissue samples (100–150 mg) were thawed on ice and homogenized in 2 mL of chilled, nuclease-free homogenization buffer. The buffer composition included 10 mM Tris (pH 8), 250 mM sucrose, 25 mM KCl, 5 mM MgCl<sub>2</sub>, 0.1 mM DTT, protease inhibitor cocktail (1×, 50× stock in 100% ethanol, G6521, Promega), 0.2 U/μL RNasin Plus (N2615, Promega), and 0.1% Triton X-100. Homogenization was carried out using a dounce tissue grinder with loose and tight pestles (20 strokes each; 357,538, Wheaton). The nuclei solution was filtered sequentially through 70 μm and 30 μm strainers. Tubes and strainers were rinsed with an additional homogenization buffer to achieve a final volume of 6 mL. The filtered solution was centrifuged at 900 rcf for 10 min, after which the supernatant was discarded, leaving 50 μL of buffer above the pellet. The pellet was resuspended in 200 μL homogenization buffer, yielding a final volume of 250 μL. Next, the suspension was mixed 1:1 with 50% iodixanol (OptiPrep Density Gradient Medium, D1556, Sigma) prepared in 60 mM Tris (pH 8), 250 mM sucrose, 150 mM KCl, and 30 mM MgCl<sub>2</sub>. This mixture was carefully layered over 500 μL of 29% iodixanol in a 1.5 mL tube and centrifuged at 13,500 rcf for 20 min. Following centrifugation, the supernatant was gently removed to avoid disrupting the pellet. The pellet was resuspended in 50 μL of chilled, nuclease-free blocking buffer containing 1×PBS, 1% BSA, and 0.2 U/μL RNasin Plus. This suspension was

transferred to a fresh tube, brought to a total volume of 500 μL with blocking buffer, and prepared for fluorescent activated cell sorting (FACS). For neuronal enrichment, 1 μL of NeuN antibody (1:500, Millimark mouse anti-NeuN PE conjugated, FCMAB317PE, Merck) was added to the samples, which were incubated on ice in the dark for 30 min. After centrifugation at 400 rcf for 5 min, the supernatant was discarded, leaving approximately 50 μL of buffer above the pellet. The pellet was resuspended in 500 μL of blocking buffer, passed through a 20 μm filter into FACS tubes, and stained with 1 μL of DAPI (0.1 mg/mL, D3571, Invitrogen) prior to sorting.

### Fluorescent-activated nuclei sorting

The nuclei suspension was maintained in darkness throughout the sorting process, which was developed using a flow cytometer (either BD FACSAria Fusion or BD FACSAria III) at 4 °C. Gating was performed based on DAPI and phycoerythrin signals, separating the nuclei into two distinct populations: NeuN<sup>+</sup> and NeuN<sup>-</sup>. Each sorted population was collected into separate tubes containing 50 μL of blocking buffer, with sorting continued until approximately 200,000 nuclei per population were obtained. Following sorting, the nuclei populations were centrifuged at 400 rcf for 4 min. The supernatant was carefully removed, leaving approximately 30 μL of buffer to resuspend the pellet. The samples were kept on ice to preserve their integrity for subsequent analysis.

### Library preparation

Library preparation from the sorted nuclei suspensions was carried out using the Chromium Next GEM Single Cell 3' Reagent Kit v3.1 (PN-1000268, 10× Genomics). Nuclei populations were manually counted, and their concentrations were adjusted to a range of 200–1700 nuclei/μL. Following the manufacturer's protocol (CG000204 Rev D, 10× Genomics), reverse transcription (RT) mix was added to the nuclei suspensions. For library preparation, samples were either loaded into separate lanes on the Chromium Next GEM Chip G (PN-1000120, 10× Genomics) for each population (targeting a recovery of 5000 nuclei per population) or mixed prior to loading, with proportions of 70% NeuN<sup>+</sup> and 30% NeuN<sup>-</sup> nuclei (targeting a recovery of 5000 or 7000 nuclei). Subsequent cDNA synthesis and library preparation were conducted in accordance with the manufacturer's instructions, utilizing the Single Index Kit T Set A (PN-1000213, 10× Genomics). Quality control and quantification steps within the protocol were performed using the Agilent High Sensitivity DNA Kit (5067–4626, Agilent Technologies) and the KAPA Library Quantification

Kit (2700098952, Roche) to ensure the accuracy and reliability of the prepared libraries.

## Illumina sequencing

Pooled libraries were prepared by combining up to 19 samples for a target nucleus recovery of 5000 or up to 16 samples for a target recovery of 7000 nuclei. Sequencing was conducted on a NovaSeq S6000 platform using an S4–200 (v1.5) flow cell with eight lanes, employing a 28–8–0–91 read configuration. The sequencing was carried out at the National Genomics Infrastructure in Stockholm, Sweden.

## sn-RNA-seq data analysis

### Pre-processing

Raw single-nuclei RNA sequencing (sn-RNA-seq) data were processed into count matrices using Cell Ranger (v3.0.0, 10× Genomics). The sequencing reads were aligned to the hg38 genome (GRCh38.p5; NCBI:GCA\_000001405.20), incorporating both intronic and exonic sequences during the alignment process.

### Quality control

To identify potential doublets, we used Scrublet [84] for each sample individually, conducting 100 iterations with automated threshold detection, default parameters, and a fixed random seed. Nuclei identified as doublets in more than 10% of the Scrublet runs were excluded. Quality control based on the distribution of unique molecular identifiers (UMIs) and unique genes detected per nucleus was then performed. Nuclei with fewer than 500 UMIs or 1200 genes were removed, as were those with more than 250,000 UMIs, over 15,000 genes, or exceeding 10% mitochondrial content. For the remaining nuclei, we modeled the logarithmic relationship between the number of unique genes and UMIs as a second-degree polynomial function. Nuclei exhibiting significant deviations from the polynomial fit—defined as a difference greater than 2000 between log-transformed gene counts and the predicted value based on UMI counts—were classified as outliers and excluded. In addition, nuclei expressing high levels of marker genes corresponding to multiple cell types were removed. To assess this, a cell type score was calculated for each subtype (Oligodendrocytes, Microglia, OPCs, Neurons, Astrocytes, Vascular cells) for each nucleus, based on the mean expression of canonical marker genes. The score distributions were evaluated across the dataset, revealing bimodal patterns in all cases. These distributions were modeled as Gaussian mixtures, and a threshold was set at the mean of the lower Gaussian distribution plus four standard

deviations. Nuclei exceeding the threshold for multiple cell types were classified as doublets and excluded. To further reduce contamination from neighboring regions, such as the claustrum or amygdala, nuclei expressing regional marker genes (*NEUROD2*, *TMEM155*, *CARTPT*, *SLC17A7*) were removed, with markers derived from the Allen Brain Atlas [32]. The number of nuclei excluded at each stage of this filtering process is summarized in Supplementary Fig. 1.

### Oligodendrocytes detection

Count matrices were analyzed using Scanpy [82] to facilitate clustering and cell type annotation, with a focus on identifying oligodendroglia. Principal component analysis (PCA) was performed, and a neighborhood graph was computed using the first 30 principal components (PCs). Clustering was conducted using the Louvain algorithm at a resolution of 0.2. The resulting clusters were annotated as either glial cells or neurons based on the expression profiles of canonical marker genes:

Astrocytes—*AQP4*, *ADGRV1*

Microglia—*CSF1R*, *FYB1*

Oligodendrocytes—*MBP*, *MOG*, *MAG*

OPCs—*PTPRZ1*, *PDGFRA*, *VCAN*

Vascular cells—*EBF1*, *ABCBI*, *ABCA9*

Neurons—*MEG3*

Oligodendrocytes and OPCs were selected, and genes were filtered based on their expression per cell. Genes detected in less than three cells were removed (1389 genes).

### Oligodendroglia lineage classification

Oligodendroglia nuclei were projected onto the first 15 PCs calculated on their 10% of most variable genes and re-clustered using the Louvain algorithm. Harmony [43] algorithm was used to remove the batch effect and integrate the data. The function `scanpy.tl.rank_genes_groups` from Scanpy [82] was used to perform a differential expression analysis between the clusters through a Wilcoxon rank-sum test. Marker genes were selected manually from the top ranked genes (log fold change > 0.5 and *p* value < 0.05) to characterize and name each of the oligodendroglia clusters as a different oligodendroglia subclass. Markers for each subpopulation are represented in Supplementary Table 2.

### Hierarchical analysis

Hierarchical clustering of the identified subpopulations was performed using the `scanpy.tl.dendrogram` function from the Scanpy [82] package. The clustering was based on the Pearson correlation method to measure similarity between subpopulations, and the complete linkage method was applied to define the cluster structure. This approach allowed

for the visualization of relationships between subpopulations based on their transcriptomic profiles.

### Compositional analysis

The differences in cellular proportion composition between conditions and brain regions were analyzed using the single-cell compositional data analysis (scCODA), a Bayesian model specifically designed to analyze changes in compositional data, particularly from single-nuclei RNA sequencing experiments. This method accounts for the inherent dependencies in compositional data, providing more accurate insights compared to both compositional and non-compositional alternatives. scCODA has been demonstrated to outperform other approaches in this domain, as described by Büttner et al. [14].

### Module analysis

To identify specific gene modules associated with oligodendroglia subpopulations, particularly those linked to *OPALIN* expression, we applied Hotspot [20] to our subsetted dataset. Hotspot detects gene modules by leveraging co-expression patterns and analyzing single-nuclei transcriptomic data, enabling the identification of functionally related gene clusters. We used default parameters but restricted our analysis to the top 10,000 highly variable genes to focus on the most relevant features of the dataset.

### Gene set enrichment analysis

Gene set enrichment analysis (GSEA) was performed using the Python package GSEAPy (version 1.0.4). Pathways were considered significantly enriched if they exhibited a Normalized Enrichment Score (NES) greater than 0.5 and a false discovery rate (FDR)  $q$ -value below 0.05, to account for multiple hypothesis testing. The analysis was conducted using Gene Ontology (GO), Kyoto Encyclopedia of Genes and Genomes (KEGG), and Reactome databases as reference sets for pathway annotation and functional enrichment.

### GSEA superpathways

GSEA results from all comparisons were processed in Python to generate superpathways and summarize enrichment patterns. Redundant pathways across contrasts were merged, with summary metrics including mean NES, average FDR, and gene coverage calculated for each. To evaluate pathway similarity, we adapted the code from <https://github.com/ayushnoori/brainstorm/blob/master/R/pathway-clustering-functions.R> in Python, calculating Jaccard indices based on gene set overlaps, and hierarchical

clustering (average linkage, threshold = 0.8) was applied to group similar pathways. Each cluster (except for the top 10 with the highest and lowest NES, which were annotated manually) was annotated with mean values for statistics columns and gene and pathways content. To generate informative labels, we applied KeyBERT (initialized with `allennai-specter`) for unsupervised keyword extraction. Pathway names were used as input, and the top two ranked  $n$ -gram phrases (1–3 words) were selected as superpathway descriptors.

### Correlation analysis (PDAO-1/PDAO-2/MOLA ratio vs MBP)

To estimate correlations between subpopulations altered in PD (PDAO-1/PDAO-2/MOLA) and MBP values, we subsetted the data for samples showing values for all the variables (number of cells related to each subpopulation and MBP intensity). To be more precise, we calculated the percentage of cells in each sample related to PDAO-1/PDAO-2/MOLA subpopulations and we only retained samples with more than five cells associated with a subpopulation. Finally, we used Spearman correlation test with the following rationale: (PDAO-1 or PDAO-2 percentages per sample)/MOLA and MBP intensity.

### Trajectory analysis

Trajectory analysis was conducted using two complementary methods. First, StaVia [68] was applied to integrate spatial and temporal data for mapping oligodendroglia differentiation. This method utilizes higher order random walks to trace lineage pathways and identify intermediate states. We executed the function `run_VIA` with default settings, modifying only the `knn` parameter to 15 for consistency across analyses. The second method, Slingshot [69], aligns single-cell data by identifying developmental lineages and connecting clusters to predict differentiation trajectories, effectively modeling the continuous maturation of oligodendroglia. Slingshot was also run with default parameters.

### Factor analysis

To investigate the genes associated with the differentiation process, we employed factor analysis using the `scikit-learn` Python package. Factor analysis is a statistical method that models observed variables as linear combinations of potential underlying latent variables, known as factors. This technique aims to identify latent structures that explain the observed variability in the dataset while minimizing noise.

In this study, factor analysis was applied to pseudotime-marked gene expression data to uncover the primary latent factors driving gene expression changes during

differentiation. The input data were normalized and scaled prior to analysis to ensure consistency and comparability across genes. By leveraging factor analysis, we identified key gene sets that contribute to distinct phases of the differentiation trajectory.

### Communication analysis

With the aim of understanding the kind of communications and the quantity of them in oligodendroglia subpopulations, we used CellChat [37]. This method identifies ligand–receptor interactions across different subpopulations, constructing communication networks that reveal key signaling pathways involved in oligodendrocytes development. This analysis was developed in R, and we subsetted some populations, limiting the number of cells to 10,000 (comprising 5000 Control and 5000 PD randomly selected) in the case the number of cells of the subpopulation exceeded this number.

### Immunohistochemistry with peroxidase-DAB method

Eight- $\mu\text{m}$ -thick formalin-fixed paraffin-embedded sections from the striatum (contralateral to samples used for sn-RNA-seq and spatial transcriptomics) at the level of the nucleus accumbens were immunostained in a Leica BOND RX fully automated research stainer using the BOND kit (Leica Biosystems, DS9800). Primary antibodies and concentrations were as follows: mouse anti- $\alpha$ -syn clone LB509 (Thermo Fisher Scientific Cat# 18–0215, RRID:AB\_2925241, 1:200), mouse anti-myelin basic protein (MBP) amino acids 129–138 clone 1 (Millipore Cat# MAB382, RRID:AB\_94971, 1:250), and rabbit anti-tyrosine hydroxylase (TH) polyclonal (Cell Signaling Technology Cat# 2792, RRID:AB\_2303165, 1:100). The immunohistochemistry protocol included bake and dewax steps, a 20-min-long heat-induced epitope retrieval (with ER2 solution for  $\alpha$ -syn and with ER1 solution for MBP and TH), and hematoxylin counterstaining. Sections were coverslipped with Permount mounting media and whole-slide images were obtained under the 40 $\times$  objective (numerical aperture 0.95, resolution 0.17  $\mu\text{m}/\text{pixel}$ ) of an Olympus VS120 virtual slide scanner (Olympus, Tokyo, Japan).

### Immunohistochemistry images analysis and quantification

All slide images were processed and analyzed using QuPath (version 0.4.3). Quantitative analysis focused on detecting intensity features related to MBP, as well as identifying the density of TH-positive projections from the

SNpc to the dorsal striatum and  $\alpha$ -synuclein aggregations (Lewy bodies/neurites, LBs/LNs). For each image, random regions of interest (ROIs) were selected within the putamen and caudate nucleus. TH-positive projections and  $\alpha$ -synuclein aggregation detection was performed independently using QuPath's pixel classifier tool. Five representative samples were chosen, and within each sample, the classifier was trained using 25 TH-positive and  $\alpha$ -syn-positive annotations and 25 TH-negative or  $\alpha$ -syn-negative annotations, resulting in a total of 125 TH-positive and 125 TH-negative annotations, and 125  $\alpha$ -syn-positive and 125  $\alpha$ -syn-negative annotations for classification.

The data obtained from MBP intensity measurements, TH projections quantification, and  $\alpha$ -syn aggregate quantifications were further analyzed using the SciPy [78] Python library. A two-sample *t* test was applied to determine the *T* and *p* values for each brain region and condition. For MBP analysis, the mean of diaminobenzidine (DAB) intensity per pixel within the selected ROIs was used as the metric for quantification. TH differences were assessed by comparing the percentage of positive TH annotations, calculated as the area of TH-positive measurements, divided by the total area analyzed ( $\mu\text{m}^2$ ). Similarly,  $\alpha$ -syn differences were quantified based on the proportion of  $\alpha$ -syn-positive regions relative to the total area ( $\text{mm}^2$ ) examined in Pu or CN, respectively. In addition, Spearman's rank correlation analysis was performed to explore relationships between various feature pairs across different regions and experimental conditions.

### Spatial transcriptomics (Xenium)

#### Spatial transcriptomics platform

Spatial transcriptomic analyses were conducted using the Xenium high-plex in situ platform (10 $\times$ Genomics), which facilitates subcellular-resolution characterization of RNA within tissue sections, similarly as previously done in Garma et al. [28].

#### Gene panel design

The Xenium technology employs oligonucleotide probes designed to quantify the expression of genes in a predefined panel. For this study, a gene panel comprising 266 genes from the Xenium Human Brain Gene Expression Panel was utilized. An additional 100 genes were selected based on our sn-RNA-seq dataset, generating a custom gene panel (Xenium Custom Gene Expression Panel 51–100 (Z3DREH), PN-1000561, 10 $\times$ Genomics).

## Experimental workflow

Tissue blocks from human subjects ( $N=4$ ; including Pu and CN) were retrieved from  $-80\text{ }^{\circ}\text{C}$  storage and transferred on dry ice to a cryostat (CryoStar NX70, Thermo Scientific). Samples were mounted on the specimen holder using Tissue Tek O.C.T. Compound (4583, Sakura) and allowed to acclimate to  $-20\text{ }^{\circ}\text{C}$  within the cryostat chamber for 5 min. Tissue sections of  $10\text{ }\mu\text{m}$  thickness were obtained and placed directly within the imaging region of precooled Xenium slides ( $12\times 24\text{ mm}$ , PN-3000941,  $10\times$  Genomics). Adherence of the sections to the slides was facilitated by briefly warming the reverse side of the slides with gentle pressure, followed by immediate refreezing on the cryobar. Tissue-mounted slides were retained in the cryostat during the sectioning process and subsequently stored at  $-80\text{ }^{\circ}\text{C}$ . Downstream processing, including probe hybridization, ligation, and rolling circle amplification, was conducted at the in situ Sequencing Infrastructure Unit (Science for Life Laboratory, Stockholm), following the manufacturer's protocol (CG000582 Rev E,  $10\times$  Genomics). Background fluorescence was minimized via chemical quenching. Tissue sections were imaged using the Xenium Analyser instrument ( $10\times$  Genomics), which also facilitated signal decoding and data acquisition.

## Oligodendroglia identification

Xenium experiments provide spatial positions of all decoded reads. Therefore, the first step in processing these datasets is to segment individual cells and identify its composition. In this study, cells from Xenium experiments were defined based on default nuclear Xenium segmentation. This conservative approach minimizes the possibilities of missegmentation, as illustrated by Marco Salas et al. [45]. Segmented cells were then preprocessed using Scanpy to identify oligodendroglia. Essentially, pre-processing of the spatial dataset involved filtering out low-quality cells. Cells with fewer than 40 total counts or fewer than 10 detected genes were excluded. The data were then normalized, log-transformed, and subjected to neighbor graph construction using Scanpy's pre-processing pipeline. A UMAP embedding was generated to visualize clusters, and Leiden clustering was applied with a resolution of 0.8 to identify distinct cell populations.

Oligodendroglia clusters (clusters 0, 3, and 9) were identified based on the expression of known oligodendroglia marker gene expression (*MBP*, *OLIG1*, *OLIG2*, *PDGFRA*, among others). The selected clusters were subsetted into a new AnnData object for further analysis. Marker gene expression was visualized spatially using matplotlib and scanpy to confirm the presence and distribution of oligodendrocytes.

## Oligodendroglia cell type assignment

Cell type deconvolution was performed using the cell2location [42] package, which infers the spatial distribution of cell types by integrating sc-RNA-seq data as a reference. First, the single-cell reference dataset, generated in this study, was preprocessed to define a knowledge base of oligodendroglia cell type-specific gene expression profiles. Genes were filtered to retain those expressed in at least five cells, representing at least 3% of the total dataset, and exceeding a mean expression cutoff of 1.12. The spatial dataset, including only predefined oligodendroglia cells, was filtered to retain genes that overlapped with the single-cell reference. Cell2location's setup function was used to prepare the spatial AnnData object for model training, specifying the sample batch as a key parameter. A regression model was trained on the reference data to estimate cell-type-specific mean expression levels. The spatial data were then analyzed using the cell2location model, which was trained for 3000 epochs with a detection alpha parameter of 200 and batch size of 10,000. Posterior distributions of cell abundances were exported to generate quantitative summaries of cell type probabilities for each spatial location. The q50 quantile (median) cell type abundances were visualized and further analyzed to identify the dominant cell types in each spatial coordinate. For oligodendrocytes, additional analysis of spatial localization and confidence intervals was performed using the posterior distributions.

## Neighborhood enrichment analysis

To assess the neighborhood enrichment of oligodendrocytes, spatial interaction networks were constructed for each sample in the dataset. The AnnData object containing oligodendroglia profiled with Xenium was first subsetted by sample, and spatial neighbors were computed using Squidpy's [53] spatial\_neighbors function with a radius of  $124\text{ }\mu\text{m}$ . This process was repeated for all samples, and the resulting AnnData objects were concatenated into a unified dataset.

Neighborhood enrichment was calculated using Squidpy's nhood\_enrichment function, with the cell type annotation, defined using cell2location, as the cluster key. This analysis computes z-scores representing the degree of enrichment or depletion of specific cell types in the neighborhoods of other cell types. Visualization of neighborhood enrichment was performed using a heatmap with a diverging colormap (coolwarm), highlighting significant positive and negative interactions. Parameters such as color scale limits ( $v_{\text{max}}=200$ ,  $v_{\text{min}}=-200$ ) and figure size were adjusted to optimize clarity and interpretability. Overall, this method provides insights into the spatial interactions and organization of oligodendrocytes in their local tissue environment,

enabling a deeper understanding of their roles in tissue architecture and function.

### Module identification using hotspot

We used Hotspot [20] to identify gene expression modules in oligodendroglia profiles derived from Xenium spatial transcriptomics data. Hotspot identifies informative genes and gene modules based on how gene variation aligns with cell similarity metrics. Informative genes show expression patterns concordant with local cell similarity. In summary, we initialized Hotspot with the following parameters:

- Layer key: ‘raw’ for raw expression values.
- Model: Negative binomial (danb).
- Latent obsm key: ‘X\_pca’.
- UMI counts key: Total UMI counts per cell.

A k-nearest neighbors (kNN) graph (20 neighbors, unweighted) was created to compute gene autocorrelations. Genes with  $FDR < 0.05$  were selected as significant. Local correlations for these genes were computed using parallel processing. Gene modules were defined using a minimum threshold of five genes, with core genes meeting an FDR threshold of 0.05. Module scores for each cell were calculated and stored. Differences in module scores between PD and control groups were analyzed using the Wilcoxon rank-sum test. Violin plots visualized score distributions, with test statistics and  $p$  values annotated.

### Niche identification using NicheCompass

NicheCompass [8] was used to identify cellular domains by integrating spatial transcriptomics data across all samples. A latent graph embedding was computed using a graph convolutional network (GCN) model with categorical covariates such as replicates. NicheCompass was run for 400 epochs with regularization to optimize ligand-receptor-based niche identification. Clustering was performed on the latent embeddings using the Leiden algorithm with a resolution of 0.2. After clustering, niches with fewer than 200 cells were filtered out, leaving three robust niches, that could be annotated as white matter (WM), gray matter (GM), and vascular niches based on their expression and cellular composition. These niches were characterized by their communication program activity, spatial localization, and enriched gene targets.

### Statistical analysis

Statistical analyses were conducted using Python-based computational tools. Differential expression analysis was performed using the Wilcoxon rank-sum test, with marker

genes selected based on a log fold change  $> 0.5$  and  $p$  value  $< 0.05$ . Hierarchical clustering of subpopulations was conducted to assess similarity based on Pearson correlation. Cellular compositional differences between conditions and brain regions were analyzed using a Bayesian model designed for sn-RNA-seq data. GSEA statistical significance was assessed using permutation-based methods (a Kolmogorov–Smirnov-like statistic), which compares the observed enrichment of genes in a gene set against a random distribution. Spearman’s rank correlation was used to examine relationships between specific features, such as the percentages of PDAO-1 or PDAO-2 and MOL-A/MBP intensity. Two-sample  $t$  tests were used to compare MBP intensity, TH-positive dots, and  $\alpha$ -syn-positive areas across conditions and brain regions, generating  $T$  and  $p$  values.

Sample sizes were determined based on prior studies and experimental feasibility. Detailed statistical results and methodologies are presented in the figures and legends.

## Results

### The human dorsal striatum shows great diversity of oligodendroglia and specific associated subclasses for PD

To elucidate the genetic networks and underlying molecular changes in OLs lineage cells within the context of PD in the dorsal striatum, we isolated and sequenced individual nuclei from freshly preserved human brain tissue samples obtained from CN and Pu of  $N=27$  controls and  $N=36$  PD donors. By employing sn-RNA-seq through a well-established workflow (Fig. 1a), we obtained 200,000 individual nuclei associated with OLs lineage cells (Fig. 1c). Notably, this dataset represents the most extensive compilation of human OLs lineage cell transcriptomic information from the dorsal striatum available to date. Control and PD groups were matched by age but not by sex due to the higher prevalence of PD in men (Fig. 1c). The average number of cells per donor and striatum (including CN and Pu) was approximately 3000 (Fig. 1c). To characterize and confirm the loss of dopaminergic neuron projections and the presence of LBs/LNs in PD samples, we performed immunohistochemical analysis for tyrosine hydroxylase (TH) and  $\alpha$ -synuclein ( $\alpha$ -syn) in the contralateral CN and Pu of MADRC control ( $N=10$  ( $\alpha$ -syn),  $N=8$  (TH)) and PD ( $N=8$  ( $\alpha$ -syn and TH)) donors, (Fig. 1b, Supplementary Fig. 2), for whom formalin-fixed paraffin-embedded sections were available. The analysis of immunoreactivity revealed a significant reduction in TH immunoreactivity (Control =  $1.66 \pm 0.58$  (SEM) versus PD =  $0.21 \pm 0.05$  (SEM),  $p=0.027$ ,  $t=2.47$ ) and a marked increase in  $\alpha$ -syn immunoreactivity (Control =  $0.004 \pm 0.0017$  versus PD =  $0.01 \pm 0.002$ ,  $p=0.035$ ,

$t=2.31$ ) specifically in the Pu of PD patients (Fig. 1b, Supplementary Fig. 2), reflecting the expected loss of TH-positive dopaminergic neuron projections and the aggregation of  $\alpha$ -syn in LB/LNs in PD, respectively.

### PD-associated clusters show specific transcriptomic signatures including stress-reactive and immunological responses

After implementing a robust quality control process (Supplementary Fig. 1), we conducted an initial clustering to identify four main classes: oligodendrocyte progenitor cells (OPCs) expressed *VCAN* as marker gene; committed OPCs (COPs) expressed *GPR17* as marker gene; and mature oligodendrocytes (MOL) were identified by the expression of *MBP*, and further subdivided based on the expression levels of *OPALIN* or *SLC5A11* marker genes (Fig. 2b). These classes were represented in both control and PD as well as in CN and Pu (Fig. 2a, b, Supplementary Fig. 3). Subsequently, cell classes were sub-clustered identifying 15 distinct subpopulations. Due to their clear enrichment in PD, we annotated some of these as PD-associated (PDA) (Fig. 2b, d). OPCs displayed four subclasses: OPCs-A (expressing the gene markers *VCAN/GPC6/SGCZ*), PDAOPCs (*VCAN/MT3/CD81*), OPCs-C (*VCAN/SEMA3E/GRIA4*), and OPCs-D (*VCAN/ST18*). MOLs expressing *OPALIN* comprised five subpopulations: MOL-A (*LAMA2/KIF6*), MOL-B (*FTH1/CRYAB/DMD*), PDAO-1 (*DBNDD2/FTL/HSPA1A*), PDAO-2 (*CTNNA2/ARHGAP24*), and MOL-F (*LURAP1L-AS1, LINC00609, LINC01608*). Within the *SLC5A11*<sup>+</sup> population, distinctions were made between PDAO-3 (*ACTN2/MT-ND3*) and MOL-G (*LINC01505, PLEKHG1, SLC25A29*) (Fig. 2b, c). The identified subpopulations represent a continuum; therefore, they do not correspond to distinct OL subtypes, but rather reflect different states within a specific subpopulation, exemplified by either different stages of differentiation or activity specialization. This is particularly evident in MOLs, where most subpopulations share common markers, with their key distinction lying in their gene expression levels rather than in the presence or absence of specific markers. These findings suggest that transcriptomic variability within MOLs is mainly driven by different functional states rather than by the emergence of discrete cell types.

After identifying distinct subpopulations within the OLs lineage, we characterized each by differential gene expression analysis (Fig. 2c, Supplementary Table 2). Of note, the disease-specific clusters (PDAOPCs, PDAO-1, PDAO-2, and PDAO-3) exhibited upregulated expression of heat shock proteins (HSP) families 70 and 90, including *HSPA1A*, *HSPB1*, *HSP90AB1*, *HSPA1B*, *HSPA8*, *HSP90AA1*, and *HSPA5*, as well as *CRYAB* and *DNAJ* family members. Thus, the elevated levels of these chaperone genes

in PDAO-1 and PDAO-2 subpopulations underscore an enhanced cellular response to stress and their involvement in protein folding and proteostasis processes within the OLs lineage (Fig. 2c).

To assess the potential disease and region specificity of these subclasses, we conducted a compositional proportion analysis using scCODA. In Pu, PD samples exhibited modest increases in PDAO-1 (+5.6%), PDAO-2 (+1.5%), PDAO-3 (+3.0%), and PDAOPCs (+2.3%), alongside a reduction in MOL-A (-9.1%) and MOL-F (-3.7%) (Fig. 2d). Notably, these PD-induced alterations were only significant in Pu, although the same tendency was observed in CN (Fig. 2d). Thus, in the striatum, particularly in the Pu, a subset of OLs exhibit a prominent stress response in PD (Fig. 2d). Furthermore, to control for potential sex-related effects, we performed a similar compositional proportion analysis stratified by sex and found no significant differences between males and females in any of the identified subpopulations, suggesting that the observed changes are independent of sex (Supplementary Fig. 4).

We next focused on *OPALIN*<sup>+</sup> MOLs as they showed to be the most affected class with three altered populations in PD (Fig. 2b, d). To confirm the gene markers associated with the *OPALIN*<sup>+</sup> subpopulations, including PDAO-1 and PDAO-2, and identify gene co-expression patterns and cellular programs associated with those gene markers, we performed Hotspot analysis. This analysis revealed several gene modules, of which Modules 4 (genes *KCNIP4, RBFOX1*) and 5 (*MDGA2, CNTN1, LUZP2, FRY, GRIK2*) were associated with immature OLs-A (immOL-A) and immature OLs-B (immOL-B), respectively. Interestingly, Modules 10 and 14, increased in MOL-A, included mitochondrial genes and genes regulating projection development (*GRID2, ZFPF2*), respectively. PDAO-1 showed increased expression of Modules 1 and 2, which were associated with HSP genes (*CRYAB, FTH1, FTL, HSPA1A, HSPA1B, HSPH1*), while PDAO-2 was linked to Modules 6 and 13, which are enriched in response to cytokines and antigen processing and presentation (*ETV5, QDPR, ARHGAP24, CTNNA2*) (Supplementary Fig. 5).

### Disrupted myelination and key pathways in parkinson's disease-associated oligodendrocyte subpopulations

In light of the significant changes observed within the mature OLs associated with PD (included in the *OPALIN* + and *SLC5A11* + subclasses), we conducted a GSEA on the most affected subpopulations, employing established databases such as GO, KEGG, and Reactome, to better understand the functional pathways implicated in PD. Our analysis focused on four key comparisons based on the compositional and

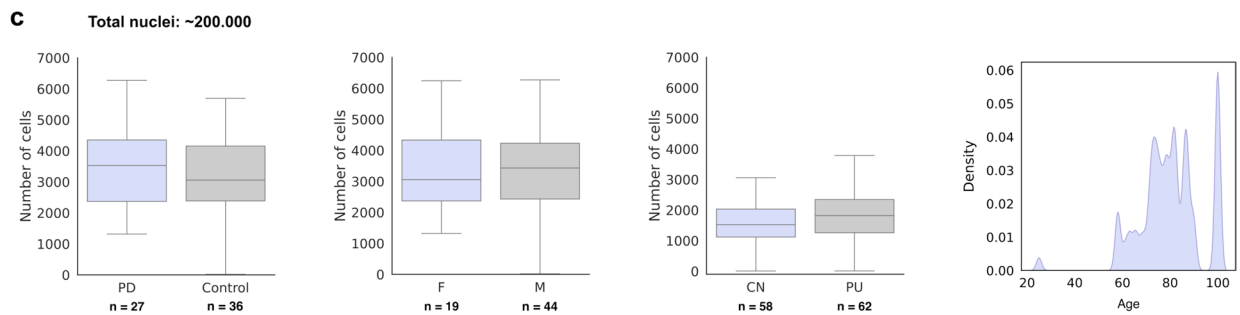
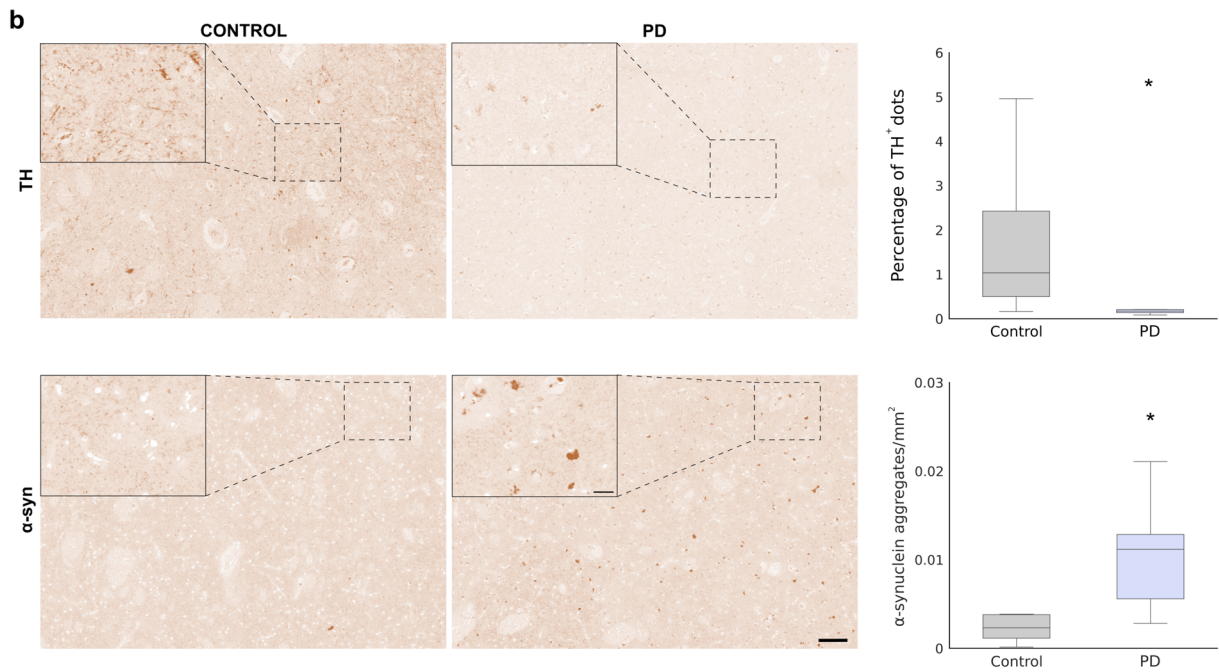
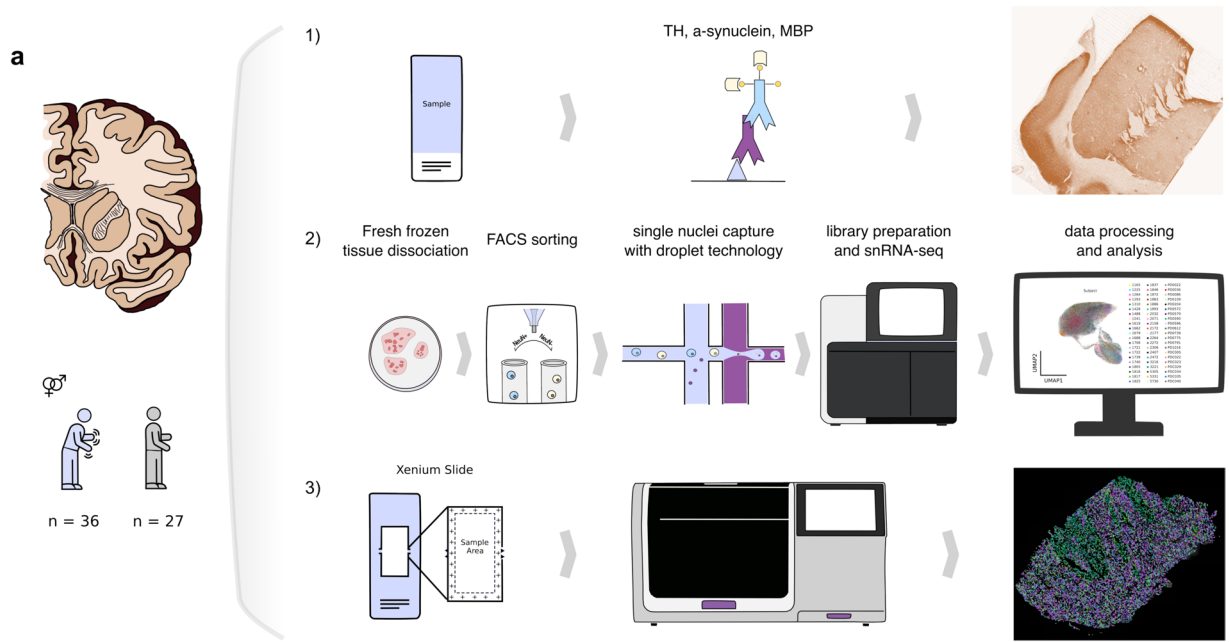


**Fig. 1** Experimental design and quantitative analysis of TH and  $\alpha$ -synuclein in the Putamen. Schematic overview of the experimental design (a). Immunohistochemical analysis of tyrosine hydroxylase (TH) and  $\alpha$ -synuclein ( $\alpha$ -syn) in the putamen. Box plots illustrate the distribution of marker expression in control and Parkinson's disease (PD) conditions. Statistical significance was determined using two-sided *t* tests, with significance indicated with an asterisk (TH analysis:  $p=0.027$ ,  $t=2.47$ ;  $\alpha$ -syn analysis:  $p=0.03$ ,  $t=2.39$ ). Scales are set at 100  $\mu$ m for low power images and at 20  $\mu$ m for insets (b). Quantitative analysis of sequenced nuclei for OLs and OPCs, categorized by condition, sex, and region, along with the age distribution frequencies of the subjects (c)

dendrogram analyses: MOL-A vs PDAO-1 and 2, PDAO-3 vs MOL-F, and PDAOs vs OPCs-A, based on OPALIN, SLC5A11, and PDGFRA expression levels. To integrate the pathway information across conditions, identified pathways were grouped into superpathways based on their gene composition similarity (Fig. 3a, b). This approach enabled a broader understanding of the biological processes that define each cellular state or subpopulation.

Overall, PDA subpopulations were primarily associated with mitochondrial activity and proteostasis, encompassing functions such as translation, ribosome biogenesis, protein folding, stress responses, and metabolic regulation (Fig. 3b, Supplementary Table 3). These were accompanied by signatures of apoptosis and immune-related pathways. In contrast, enriched control subpopulations were associated with superpathways involved in neural development, including regulation of neurogenesis, synapse assembly, dendritic morphogenesis, and signaling mechanisms related to ion transport, cell adhesion, and cellular differentiation within the nervous system (Fig. 3b).

Within this general framework, distinct functional specializations emerged across specific comparisons. For instance, PDAO-1 exhibited an upregulation of cellular stress and immune responses, particularly those involving protein modification, cell cycle control, and pro-inflammatory signaling (Supplementary Table 3). PDAO-2, by contrast, was marked by enhanced innate immune signaling and apoptotic pathways mediated by DAPI2 and interferon responses (Supplementary Table 3). Meanwhile, MOL-A demonstrated a unique molecular profile involving glycosphingolipid metabolism, TRP channel signaling, transcriptional regulation, and specialized functions like myelination and ciliary transport (Supplementary Table 3).

PDAO-3 revealed a metabolic profile, including pathways for steroid and lipid biosynthesis, intracellular and organelle-specific processes, signaling networks, and stress-related transcriptional regulation (Supplementary Table 3). In parallel, MOL-F was characterized by upregulation in nucleotide metabolism, cholesterol biosynthesis, calcium signaling, and gene expression pathways linked to MET-PTK2 and TAZ signaling axes (Supplementary Table 3).

Lastly, the dysregulated PDAOs presented an enrichment in adaptive immune signaling, antigen receptor regulation, and DNA repair mechanisms, pointing to roles in host defense, autoimmunity, and immune tolerance (Supplementary Table 3). In contrast, the healthy OPC-A subpopulation showed increased activity in signaling regulation, transcriptional control, vesicle transport, ion homeostasis, synaptic function, and structural remodeling within the neuronal system (Supplementary Table 3).

Furthermore, to assess the impact of PD on myelin quantity, we conducted a quantitative immunohistochemistry analysis using the MBP marker, which is indicative of myelination levels (Fig. 3c). The results revealed a decrease in MBP immunoreactivity within the Pu in PD vs control donors (control =  $0.21 \pm 0.01$ , PD =  $0.17 \pm 0.009$ ,  $p$  value =  $0.047$ ,  $t=2.11$ ) (Fig. 3d). In addition, to further elucidate the relationship between MBP immunoreactivity in the Pu and the relative abundance of OLs subpopulations, we conducted a correlation analysis between MBP immunoreactive signal and the ratios of PDAO-1 and PDAO-2 to MOL-A, reflecting the aforementioned shifts in cell population proportions in PD. We observed a significant negative correlation, indicating that as the ratio of PDAO-1/MOL-A ( $r=-0.56$ ,  $p$  value =  $0.02$ ) and/or PDAO-2/MOL-A ( $r=-0.51$ ,  $p$  value =  $0.02$ ) increases (suggesting a shift of MOL-A to PDAO-1 and/or PDAO-2), MBP levels decrease (Fig. 3e, f).

### Trajectory inference reveals disrupted oligodendrocyte differentiation pathways in Parkinson's disease

To understand the normal differentiation process and identify deviations from normality associated with PDAOs clusters in PD, we conducted trajectory inference analyses using the VIA and Slingshot algorithms. To infer the normal differentiation pathway, we considered all OL clusters except PDAOs, with samples from both conditions and regions. The differentiation process we identified is as follows: precursor cells, specifically OPCs-A, represent the original state and undergo differentiation into OPCs-C. These then further mature into COPs and immOL-B. Subsequent differentiation toward MOLs progresses through MOL-A and MOL-B populations, which are implicated in the initiation of myelination, as evidenced by the expression of Laminin-2 (*LAMA2*) and other cell adhesion molecules (CAMs). As differentiation advances, the MOL-F population emerges, characterized by the expression of genes associated with cholesterol metabolism, a process critical for the myelin sheath wrapping characteristic of mature oligodendrocytes (Fig. 4a). Intriguingly, we identified a previously unreported branch in the differentiation trajectory (Supplementary

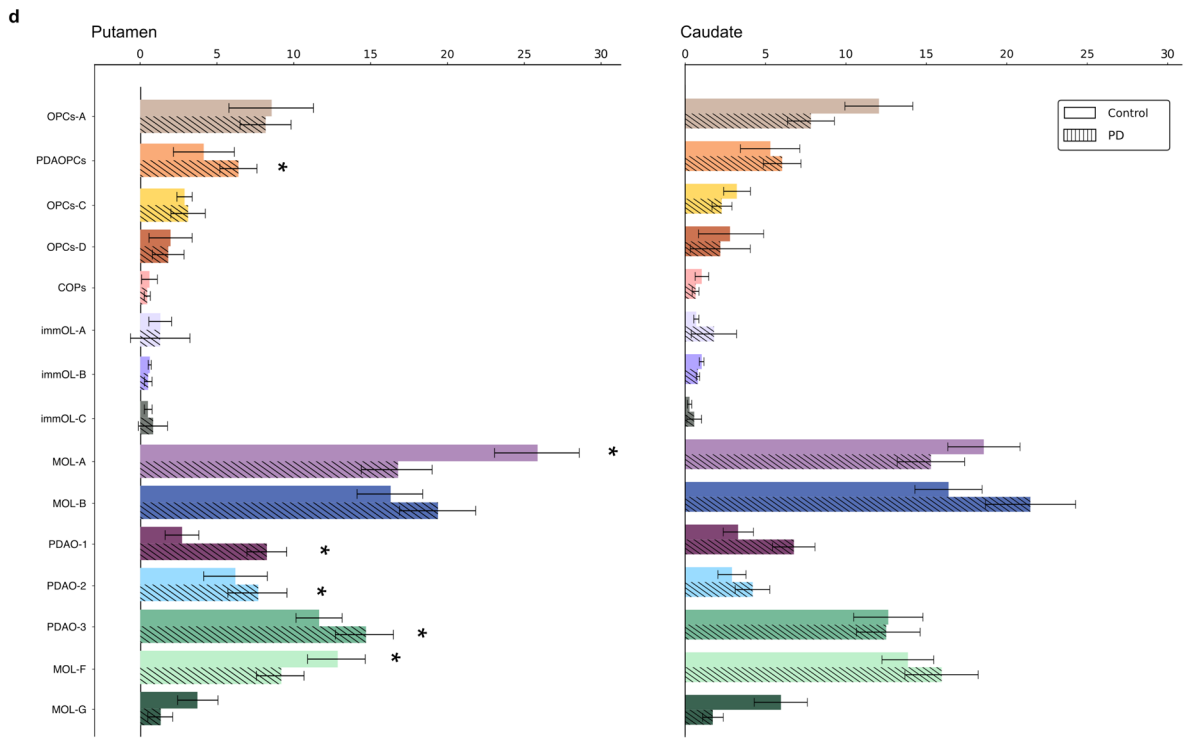
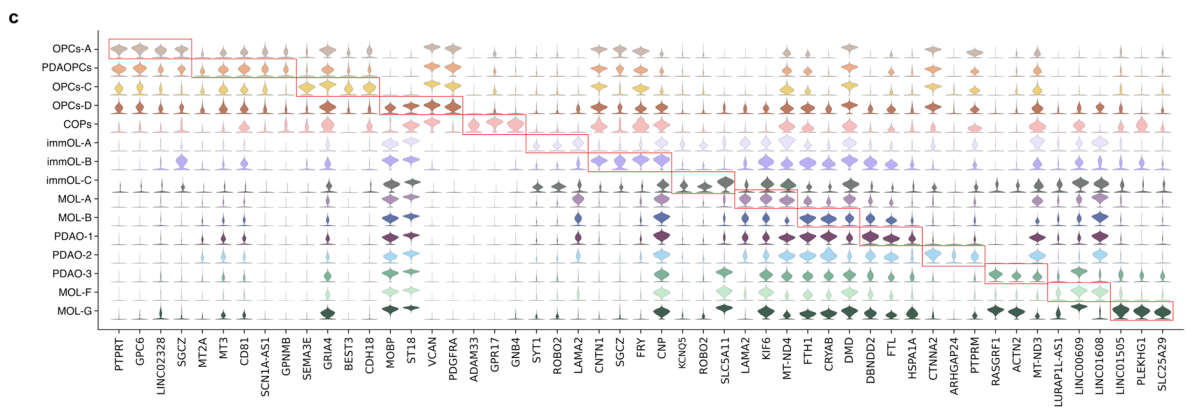
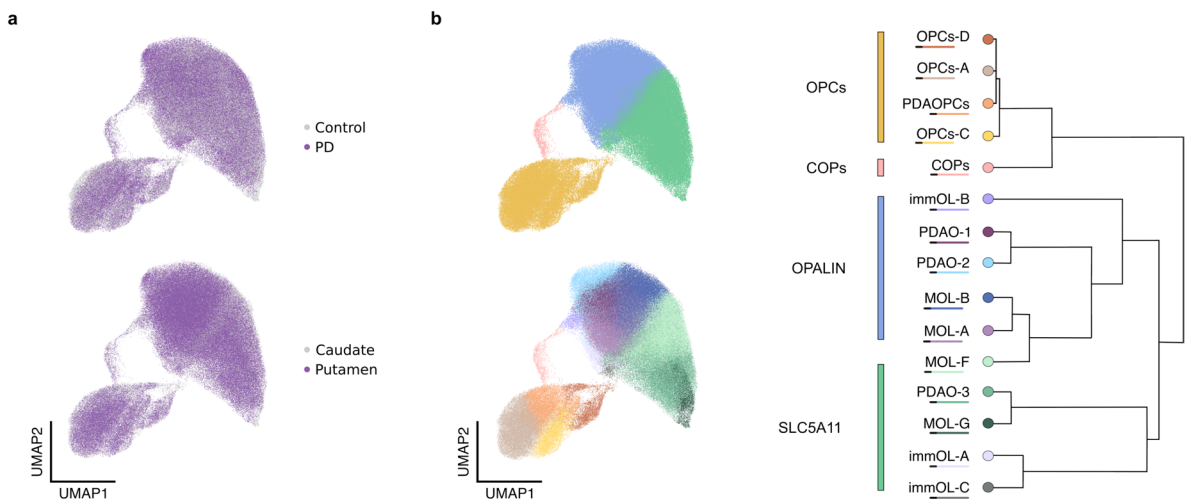


**Fig. 2** Quantitative analysis of oligodendrocytes and OPCs subpopulations. UMAPs display the uniform distribution of cells from each region and condition across all subpopulations (a). UMAP representing principal oligodendrocyte (OL) and oligodendrocyte progenitor cells (OPC) classes: OPCs, COPs, MOLs-*OPALIN*<sup>+</sup>, MOLs-*SLC5A11*<sup>+</sup> (b, Top Left). UMAP visualization depicting OLs and OPCs subpopulations, with distribution within subclasses based on transcriptomic similarity (b, Bottom Left), as illustrated in the dendrogram (b, Right). Stacked violin plots representing marker expression profiles for each subpopulation (c). Bar plots showing the percentages of each subpopulation, calculated based on the total number of nuclei in each condition (d). Asterisks (\*) indicate significantly altered populations based on scCODA *p* value of confidence (<0.2)

Fig. 6): OPC-D transitions through immOL-C to immOL-A, ultimately converging toward MOL-A/MOL-F. Moreover, immOL-C is also linked to MOL-E, suggesting a potential alternative pathway facilitating direct differentiation and maturation processes (Fig. 4a).

When analyzing all the clusters, including those PDAOs, and samples from both conditions and regions, we observed deviations in this normal differentiation trajectory. PDA clusters appeared to originate from specific healthy populations, exhibiting altered differentiation pathways in the diseased striatum. Specifically, PDAO-1 likely emerged directly from MOL-A in PD striatum, reflecting a disruption in the normal differentiation pathway of MOL-A to MOL-B and MOL-F. PDAO-2 showed a more ambiguous origin, potentially involving disruptions at the MOL-A and/or immOL-B differentiation stages, indicative of a complex pathological process (Fig. 4c). In the case of PDAO-3, it appeared to arise from perturbations in MOL-F, suggesting PD-associated alterations in this late-stage differentiation population. Finally, the same applied to PDAOPCs, which originated from OPCs-A, highlighting disruptions in the earliest stages of OL lineage differentiation.

To further investigate the molecular mechanisms underlying these differentiation pathways, we applied factor analysis to pseudotime-ordered gene expression data, which enabled us to identify distinct genetic signatures underpinning the differentiation trajectories (Fig. 4c, Supplementary Table 4), highlighting potential molecular mechanisms involved in disease-associated alterations. Factor analysis revealed specific genetic signatures involved in the transitions observed in normal differentiation, including genes critical for myelination, cholesterol metabolism, and cell adhesion (*LAMA4*, *LAMA2*, *MOBP*, *ERBB4*). When applied to pathological trajectories, factor analysis highlighted specific gene dysregulations associated with PDA clusters, providing insights into molecular mechanisms disrupted by disease (Fig. 4c). These findings underscore the role of aberrant gene regulation in driving pathological deviations from normal OL differentiation.

## Altered intercellular interactions and neurotransmitter signatures in Parkinson's disease-associated oligodendrocyte subclasses

We further aimed to examine potential intercellular communication among the identified subpopulations and to determine whether communication patterns differ between control and PD striatum. With CellChat, we evaluated outgoing and incoming signaling dynamics based on the expression of known ligand–receptor pairs across subpopulations. Our results revealed significant disruptions in communication patterns within PD-associated clusters. Specifically, the analysis demonstrated a marked reduction in the expression of extracellular matrix (ECM) and adhesion molecules genes, such as *NCAM*, *CADM*, Laminin, and *CDH1*, in PDAO-1 compared to MOL-A, the latter exhibiting the highest expression levels of these molecules within the *OPALIN*<sup>+</sup> class (Fig. 5a, b). These findings suggest a weakening of adhesion and ECM-mediated signaling in PDAOs subpopulations. Indeed, there was a sharp decline in outgoing signals linked to myelination, particularly those associated with Laminin (*LAMA2*), in both PDAO-1 and PDAO-2. Furthermore, critical cell adhesion molecules (e.g., *NCAM*, *CADM*, and *CDH1*) were nearly absent in PDAO-1, highlighting substantial deficits in the ability of this cluster to engage in adhesion-based communication, likely contributing to the broader dysregulation of cellular networks in PD (Fig. 5b).

In contrast, cholesterol-related molecules, particularly within the *SLC5A11*<sup>+</sup> class, were elevated in these subpopulations (PDAO-3, MOL-G), aligning with the distinct biological profile of these populations demonstrated with hierarchical clustering, annotation, and GSEA analyses. Notably, the PDAOPCs subpopulation exhibited the lowest levels of general communication molecules among precursor cells, further suggesting disrupted intercellular interactions in early-stage OL precursors in PD (Fig. 5b).

Another striking finding from the CellChat analysis was the distinct upregulation of glutamate-related signaling molecules in OPC subpopulations, particularly in PDAOPCs. This observation prompted a deeper investigation into neurotransmitter signaling profiles across OL subpopulations (Fig. 5c). While the most pronounced differences were observed between OPCs and MOLs, key neurotransmitter-associated genes were also found to be differentially expressed in PD-specific clusters. For instance, *CHRNA10* and *GABRG1* were highly expressed in PDAO-2, while *GABRR2* was significantly upregulated in both PDAO-1 and PDAO-2. These findings point to a distinct alteration in neurotransmitter signaling in PD-associated OLs, likely contributing to their functional deficits.

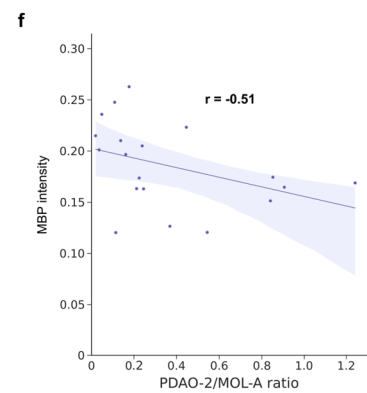
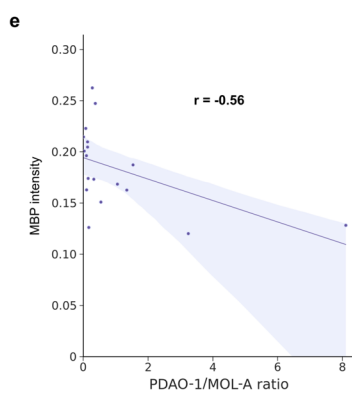
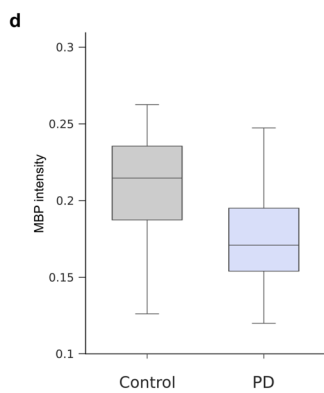
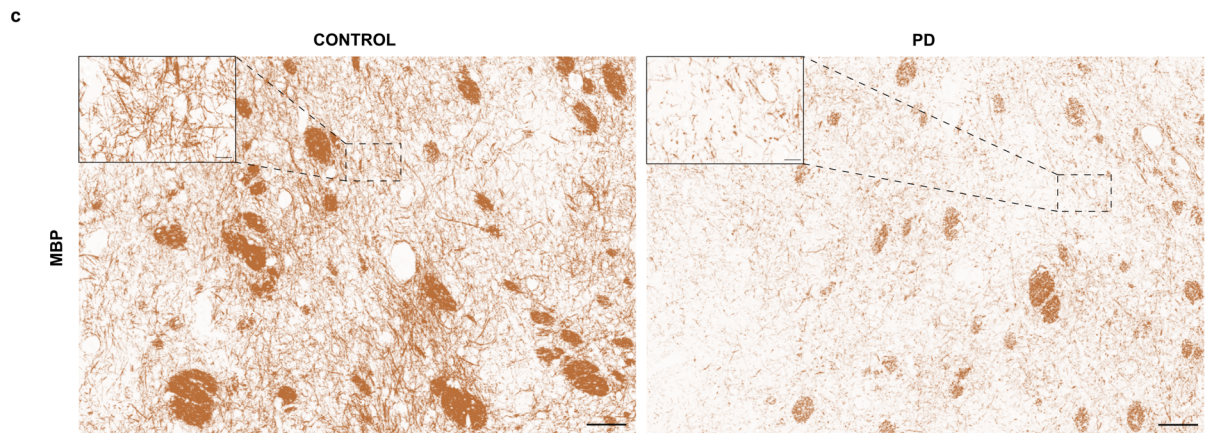
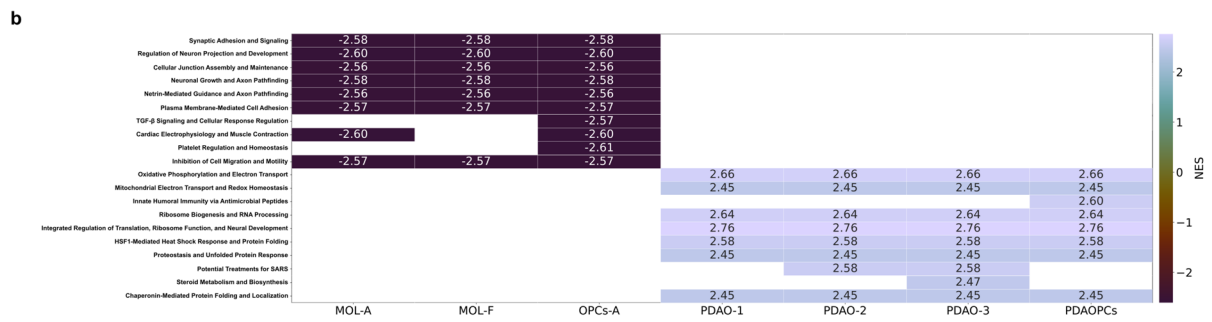
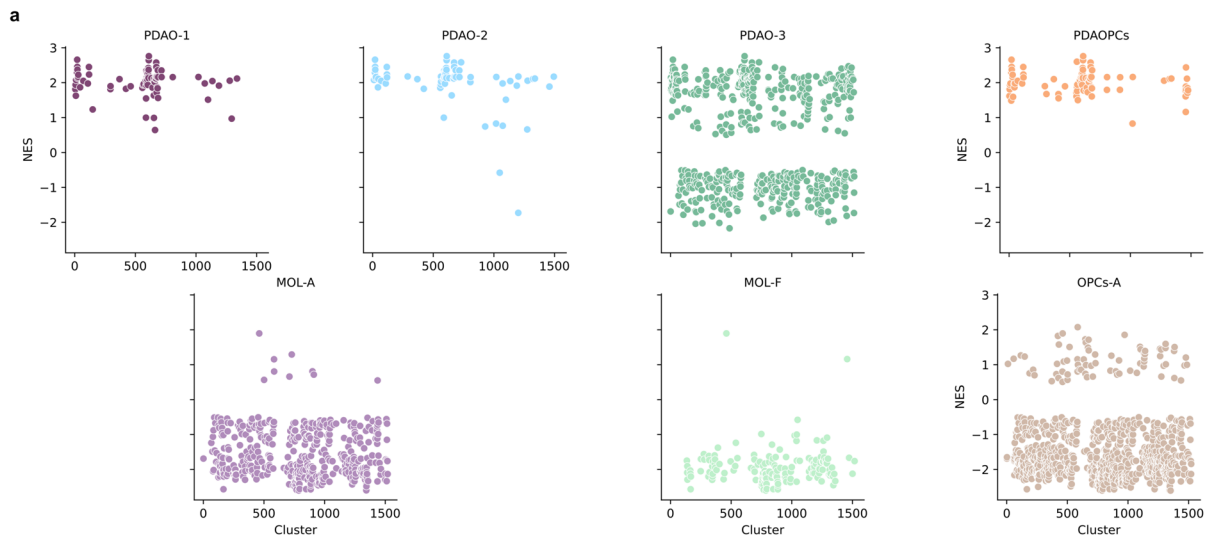


**Fig. 3** Gene Set Enrichment Analysis and MBP expression in PD-associated oligodendrocytes subpopulations. Each panel displays Normalized Enrichment Scores (NES) for clusters/superpathways derived from GSEA results, grouped by the cell type in which they are upregulated and based on the comparison they are related to (PDAO-1 vs MOL-A, PDAO-2 vs MOL-A, PDAO-3 vs MOL-F, PDAOPCs vs OPCs-A). Dot plots within each facet represent NES values per cluster for that specific cell type. Superpathways were filtered based on an FDR < 0.05 and an absolute NES value > 0.5 (a). Heatmap illustrates the distribution of NES values obtained from GSEA superpathways across the studied subpopulations for the top 20 clusters, including the 10 most positively and 10 most negatively enriched clusters based on NES magnitude. Rows represent GSEA-derived superpathways, while columns correspond to subpopulations of interest. Each cell reflects the NES for a given superpathway-cell type combination, with the color gradient indicating the level of enrichment (b). Immunohistochemical analysis of MBP in the Pu region under control and PD conditions. Scales are set at 100  $\mu$ m for the low power images and at 20  $\mu$ m for their insets (c). Boxplots illustrating the distribution of MBP expression in control and PD conditions.  $p$  value = 0.047,  $t$  = 2.11 (d). Scatter plot depicting the correlation between the ratio of PDAO-1 to MOL-A cells and MBP expression.  $r$  = -0.56,  $p$  value = 0.02 (e). Scatter plot showing the correlation between the ratio of PDAO-2 to MOL-A cells and MBP expression.  $r$  = -0.51,  $p$  value = 0.02 (f)

### Spatial mapping reveals oligodendrocyte subpopulations and myelin-related alterations in Parkinson's disease

To validate the cell populations identified through sn-RNA-seq and further analyze other tissue-related variables, we employed spatial transcriptomics. This technique preserves the spatial organization of gene expression within the tissue, enabling the direct mapping of sn-RNA-seq-defined cell populations to their native anatomical contexts. By integrating these high-dimensional data modalities, we evaluated the robustness and biological relevance of sn-RNA-seq-derived clusters, ensuring that the identified populations are spatially resolved and assessing whether they localize to distinct striatal regions or whether they correspond to distinct functional domains within the same region.

Through spatial transcriptomics, we profiled 435,157 oligodendroglia cells. Using the cell2location model, we transferred sn-RNA-seq annotations to cells identified as OLs or OPCs in the spatial dataset (Fig. 6a). Analysis of the 366 profiled genes enabled the identification of all sn-RNA-seq-derived subpopulations within the OL lineage across both CN and Pu in the spatial transcriptomic dataset (Fig. 6a).

A noteworthy observation was the spatial distribution of these subpopulations within the tissue. Neighborhood enrichment analysis identified four main co-localizing subpopulations: PDAO-1, PDAO-3, MOL-F, and MOL-G (Fig. 6b). PDAO-3, MOL-F, and MOL-G were characterized by their maintenance of a myelin-related profile

and appeared to be predominantly located within the WM tracts that cross through the striatum (Fig. 6c).

To better understand the molecular changes specific to PD, we conducted a Hotspot analysis to identify distinct gene expression modules that show significant variance between control and PD donors. This analysis highlighted two key modules with notable differences: heat shock protein response (HSPR) and myelination. Specifically, we observed a significant upregulation of the HSPR module in PD, accompanied by a marked downregulation of the myelination module, pointing to opposing trends in these two pathways (Fig. 6d, e).

The HSPR module, associated with cellular stress responses, exhibited strong correlations among genes encoding heat shock proteins, including *HSPA1A*, *DNAJ1*, *HSP90AB1*, and *CRYAB*. This module showed elevated activity in PD, suggesting an amplified cellular stress response in affected cells. Importantly, the activity of the HSPR module in PD was strongly correlated with the transcriptional signatures of PDAOs, further reinforcing the robustness of this finding (Fig. 6d, e).

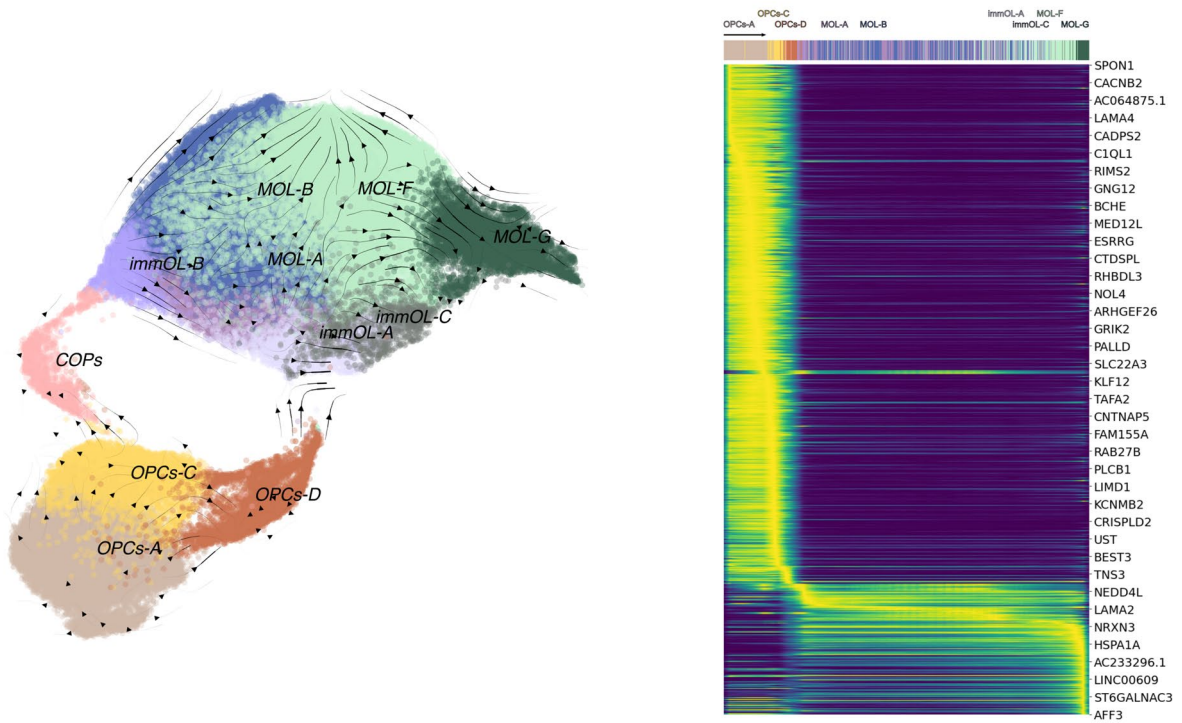
In contrast, the myelination module, which encompasses genes critical for myelin formation and maintenance, such as *MAG*, *MOBP*, and *CNTN2*, was significantly downregulated in PD, suggesting an impairment of myelination processes. The reduced co-expression among genes in this module further underscore the disruption of myelin-related pathways in PD (Fig. 6d, e).

Interestingly, the activity of the HSPR and myelination modules appeared to be inversely related. In PD samples, the increased activity of the HSPR module coincided with a decrease in the myelination module, suggesting a potential trade-off between cellular stress response mechanisms and the maintenance of myelin. This interplay likely reflects a previously unrecognized critical aspect of PD pathophysiology, where OL energy and/or machinery resources are likely diverted to manage stress, compromising other vital processes like myelination (Fig. 6d).

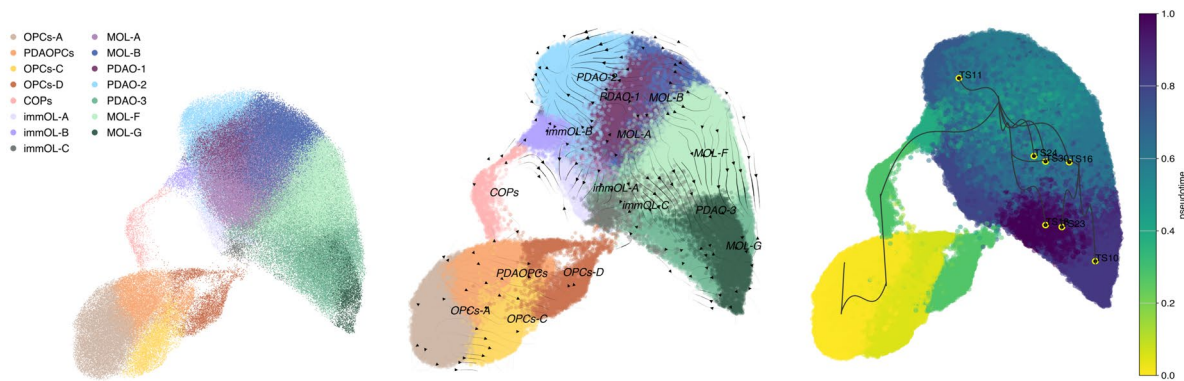
## Discussion

PD is a complex neurodegenerative disorder with no cure and unknown trigger in the vast majority of sporadic cases. Understanding the different key alterations with cell type specificity is crucial to develop treatments that can halt the progression of the disease. Traditionally, PD has been associated with dopaminergic neuron degeneration and Lewy bodies. Recently, oligodendroglia has emerged as a potential critical cell type in this disease [1, 13, 18, 64], but its involvement has not been investigated in depth. Characterizing the diversity of OLs and their precursors, as well as how they are affected in one of the most impacted

**a**



**b**



**c**

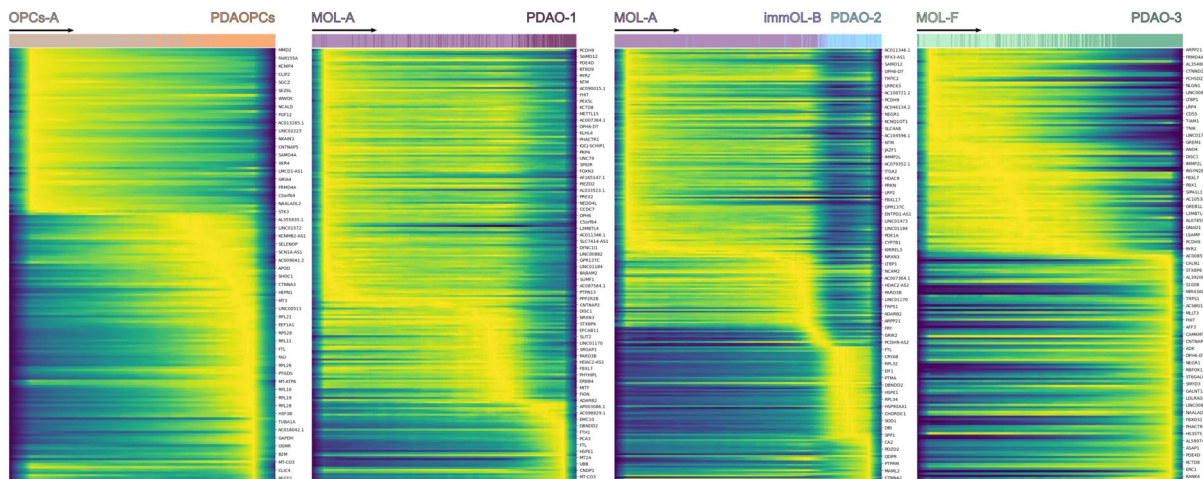


**Fig. 4** Pseudotime analysis of oligodendrocyte differentiation and divergent trajectories in PD. Pseudotime UMAP generated via t-SNE analysis, excluding the expanded populations associated with PD. Arrows depict the progression of the differentiation trajectory, which proceeds from oligodendrocyte progenitor cells (OPCs) through COPs/OPCs-D, followed by immature oligodendrocytes (immOLs), and culminating in the transition from MOL-A to MOL-G (a, Left). Heatmap illustrating the expression of key genes involved in this differentiation process (a, Right). UMAP visualizations of differentiation trajectories in PD-associated clusters. Pseudotime analysis highlights a convergence point at MOL-A, from which the differentiation diverges into PDAO-1 and PDAO-2 clusters (b). Schematic representation of genes associated with differentiation pathways, tracing potential origins and pathways leading to the development of PD-associated clusters (c)

brain regions in PD (the dorsal striatum), is essential for uncovering the mechanisms underlying oligodendroglia dysfunction and its contribution to neurodegeneration.

In this work, we have built the largest dataset, to our knowledge, of sn-RNA-seq from CN and Pu samples from PD and control donors, and applied one of the most recent and sensitive spatial transcriptomics approaches to delineate the main transcriptomic changes of oligodendroglia with their neuroanatomical correlation in this neurodegenerative disorder.

The complexity of OLs and OPCs has only recently been elucidated in specific brain regions [3, 35, 46, 74, 88]. In our study, we analyzed more than 200 K nuclei from CN and Pu of 63 donors, identifying 4 main classes and 15 distinct subclasses. The main classes (OPCs, COPs, *OPALIN*<sup>+</sup> MOLs and *SCL5A11*<sup>+</sup>) were previously described [3, 46, 54, 62, 64, 74, 88].

Among our subclasses, MOL-A and G (Int0 and Int3 in Sadick et al. [62]), and immOL-B (Int4 in Sadick et al. [62] and FRY population in Smajic et al. [64]) have been previously identified. Importantly, our large study enabled the identification of novel subclasses, including OPCs-C, OPCs-D, MOL-F, and immOL-A and C, as well as those associated with the disease, such as PDAOPCs and PDAO-1, PDAO-2, and PDAO-3. While MOL-B and PDAO-2 showed similarities with previous described populations, they have a distinct transcriptomic profile (Supplementary Table 5): PDAO-2 share similarities with the disease-associated OLs (DAOs) identified in MS by Falcão et al. [24], including pathways involved in antigen processing and presentation via major histocompatibility complex class I and II (MHC-I and -II), and immune OLs (imOLs) from Jäkel et al. [35] (related to OPC1 in Falcão et al. [24]) sharing *ARHGAP24* and *CTNNA2* among others. Thus, although DAOs have been observed in neurodegenerative diseases like MS (Falcão et al. [24]) and AD (Jäkel et al. [35]), the transcriptomic profile of PDAO-2 demonstrates unique characteristics (Supplementary Table 5), suggesting a disease-specific role in PD.

Alterations in HSPs have been associated with microglia in the midbrain in PD [64] and with specific signatures of OLs in PD [25, 64], but their role with OLs population specificity has not been previously described. The elevated expression of HSP-related genes, including *HSPA1A*, *HSPB1*, and *HSP90AB1*, along with increased chaperone-associated transcripts, highlights a potential role in stress adaptation and prevention of protein aggregation [76]. Intriguingly,  $\alpha$ -syn aggregation in OLs is the neuropathological hallmark of multiple system atrophy (MSA) but is not a feature of PD. Trajectory inference analysis indicates that PDAO-1 likely derives from the MOL-A lineage and it exhibits significant impairments in myelination-related processes compared to MOL-A, demonstrating a maladaptive response in OLs during PD progression. This includes downregulation of genes involved in myelin assembly—such as actin cytoskeleton components and adhesion molecules like laminins and cadherins as demonstrated with CellChat—and reduced neuronal communication, potentially contributing to the striatal WM alterations observed in PD. Although demyelination or remyelination failure are not established PD hallmarks, few works have pointed in that direction [10, 87] and support our findings.

PDAO-2, a distinct OL subpopulation, displays an immunological profile, including increased expression of neurotransmitter receptors (*GABRG1*, *GABRR2*) and immune-related genes (*HLA-C*, *HLA-A*). This aligns with findings that OLs can acquire immune-like functions in neurodegeneration, including antigen presentation and cytokine release [24, 35]. In PD, OL may influence microglia and astrocyte activity, contributing to the chronic neuroinflammatory environment [22, 49, 50]. Furthermore, reduced expression of myelination-associated communication molecules like Laminin [39] and Opalin [26] in PDAO-2 may indicate a shift from a supportive role in myelination toward an immunomodulatory function, as reported in other disorders like MS and AD [38, 86]. Thus, PDAO-2 may represent a dysfunctional OLs state that contributes to myelin loss and neuroinflammation in PD progression.

The negative correlation between MBP expression and the proportion of PDAO-1 and PDAO-2 underscores the critical role of OLs dysfunction in demyelination and neurodegeneration across neurological disorders, including PD [10, 17, 19, 27, 51, 87]. The increase of these subpopulations, alongside decreased MBP levels, suggests a shift in OL function away from myelination toward stress and immune responses, impairing their capacity to maintain and repair myelin and exacerbating neurodegeneration.

Two additional PD-associated subclasses, PDAO-3 and PDAO-1, were identified. PDAO-3, a mature OL population, exhibits transcriptomic alterations indicative of

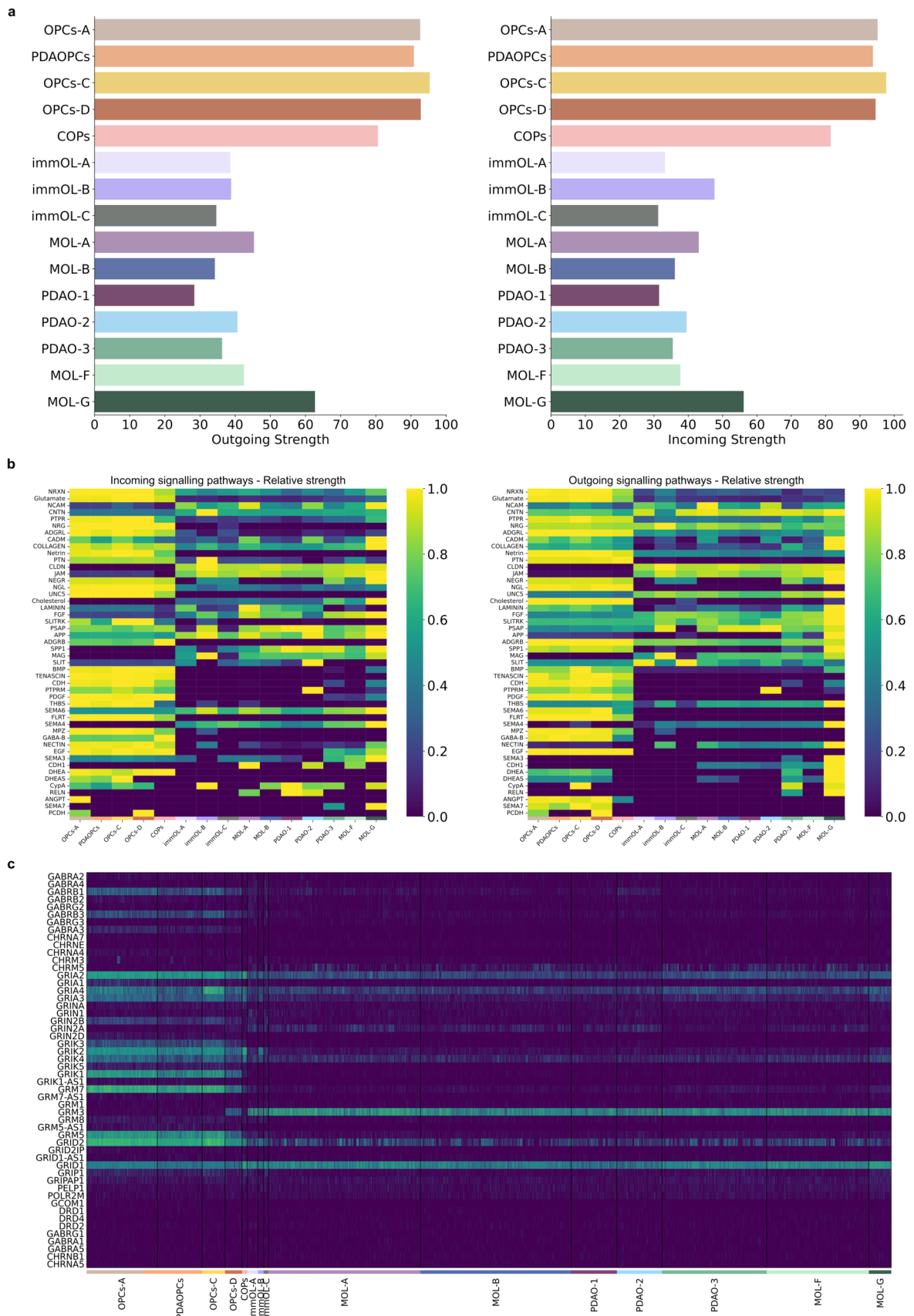


**Fig. 5** Disrupted intercellular communication and neurotransmitter signatures in PD-associated oligodendrocytes. Bar plots illustrating the outgoing and incoming communication strengths for each subpopulation, as determined by ligand-receptor interaction analysis (a). Relative signaling pathway strengths are depicted for each subpopulation, highlighting distinct communication profiles (b). Heatmap displaying the expression levels of neurotransmitter-associated markers identified in at least 50 cells within any given population, showcasing distinct molecular signatures across subpopulations (c)

dual roles in stress adaptation and impaired myelination. GSEA indicates upregulation of autophagy, sphingolipid metabolism, and cytokine signaling, concurrent with downregulation of processes like cell projection organization and integrin signaling. Spatial transcriptomics further demonstrates the enrichment of PDAO-3 in striatal WM tracts, underscoring its potential role in the myelin deficits observed in PD [33, 56], and supporting the increased expression of cholesterol-related molecules identified in this subpopulation through CellChat analysis.

PDAOPCs, a subset of OPCs, exhibit heightened activity in pathways related to mitochondrial function and mitophagy, coupled with enhanced antigen presentation capabilities, indicating an adaptive response to cellular stress and metabolic demands in the PD microenvironment. However, the reduced expression of intercellular communication molecules suggests a compromise in PDAOPCs ability to mature into myelinating OLs, likely contributing to the myelin alterations observed within Pu of PD patients. In addition, PDAOPCs exhibit a distinct glutamate-related signaling profile, implicating them in altered neurotransmitter dynamics and interactions with neuronal circuits in PD. Together, these features point to PDAOPCs as an early, vulnerable oligodendroglial population whose dysfunction propagates broader myelin and connectivity deficits in PD.

Overall, the transcriptomic changes were more prominent in Pu than CN, as illustrated by changes in OL composition, which is consistent with the more severe reduction in TH and MBP immunoreactivity in Pu versus CN, as well as increased  $\alpha$ -synuclein aggregations. These findings align with the spatio-temporal progression of the nigrostriatal pathway degeneration in PD [11, 60]. Pu is critically involved in motor control and well-established to be affected in PD [10, 17, 66], further supporting our findings and reinforcing Pu involvement in disease pathology and its critical role in motor control. However, it remains unclear whether the observed changes in OLs represent a primary pathogenic process in PD or arise secondarily due to the degeneration of dopaminergic projections. Given the selective vulnerability of dopamine terminals in Pu and the accumulation of  $\alpha$ -synuclein, it is plausible that the myelinated fibers within this region undergo secondary degeneration, triggering the transcriptional reprogramming

observed in OL subpopulations, with changes in GABA receptor expression serving as an example of how alterations in neurotransmitter levels might influence these processes. Conversely, experimental evidence demonstrates that  $\alpha$ -synuclein can transfer from neurons to OLs [59], and  $\alpha$ -synuclein inclusions were detected in OLs of PD patients [2, 79], indicating a potential primary role for oligodendroglial in PD pathology and reinforcing the presence of enriched pathways related to protein misfolding and proteostasis. The interplay between OL alterations, dopaminergic neuronal loss, and  $\alpha$ -synuclein dynamics remains unresolved; however, our data point to WM dysfunction as a potentially underrecognized component of PD-related pathology in the basal ganglia.

Importantly, determining whether the affected fibers belong to the striatopallidal (indirect pathway) or striatonigral (direct pathway) projections is crucial, as each pathway plays a distinct and opposing role in motor regulation. Further experiments and approaches are needed to determine this. Such information could clarify which component of the basal ganglia circuitry is primarily disrupted in PD in Pu, as recent studies have identified the striatopallidal route as a critical component of the basal ganglia circuitry for motor control [44], suggesting that OL-associated dysfunction within this pathway could exacerbate motor deficits. Moreover, aberrant GABAergic signaling from MSNs along these fibers may impact OL function by altering their maturation, impairing myelination, or inducing immune-like phenotypes (as in the case of PDAO-2), particularly in regions where OL–GABA interactions are spatially enriched.

Our results add to a growing body of evidence underscoring the critical interplay between glial and neuronal dysfunction in PD and suggest that oligodendroglial pathology may be a promising target for therapeutic intervention aimed at slowing or halting disease progression. Our transcriptomic analysis emerged two candidate therapeutic targets: RHO GTPase signaling and oxidative stress pathways, both of which are dysregulated in PDA OL subpopulations. Among agents modulating the RHO pathway, Fasudil, a ROCK inhibitor, is being tested in clinical trials for PD (NCT05931575) [83] and has exhibited both neuroprotective and remyelinating properties in MS [81, 83]. Moreover, Catalpol has shown neuroprotective efficacy in MPTP-induced PD models [80] attributed to its capacity to reduce oxidative stress and promote OL regeneration and remyelination [70, 80]. Furthermore, Fingolimod, an FDA-approved therapy against MS [63], has been shown to exert both neuroprotective and remyelinating effects by enhancing OL survival and function in PD-related models such as those induced by rotenone and 6-OHDA [58, 89]. Lastly, since PD is twice as common in men

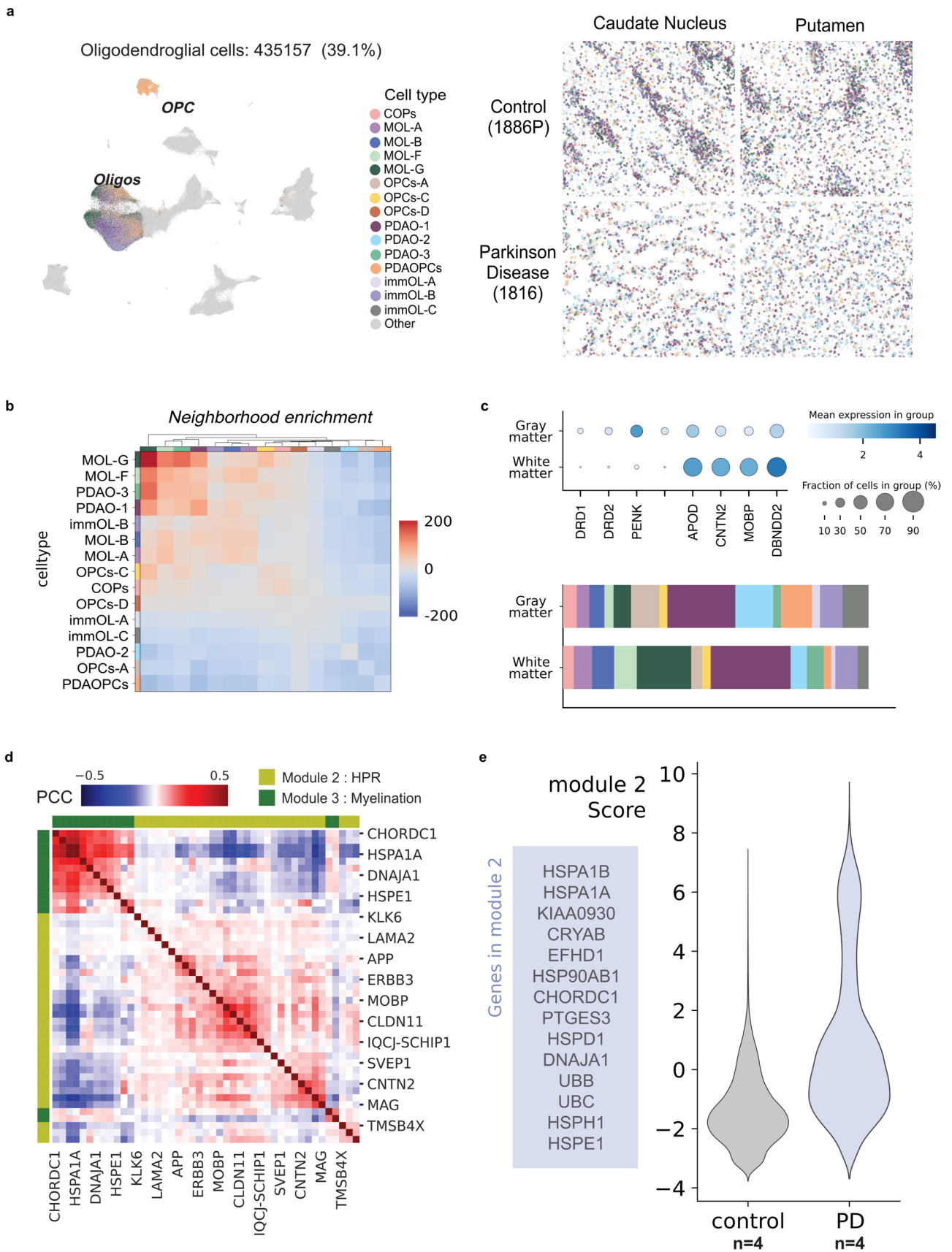


**Fig. 6** Spatial transcriptomics reveals region-specific oligodendrocyte distribution and molecular signatures in PD. UMAP illustrating oligodendrocyte populations profiled through spatial transcriptomics, corresponding to the populations identified via sn-RNA-seq (**a**, Left). Spatial distribution of oligodendrocyte subpopulations across CN and Pu (**a**, Right). Heatmap depicting neighborhood enrichment patterns for all identified subpopulations, highlighting spatial co-localization (**b**). Spatial localization of oligodendrocyte subpopulations within the gray matter (GM) and white matter (WM) areas (**c**). These regions were categorized based on marker expression (**c**, Top). Bar plots illustrate the distribution of oligodendroglia subpopulations across both GM and WM (**c**, Bottom). Heatmap represents the distribution of module 2 (heat shock protein response, HSPR) and module 3 (myelination), demonstrating a negative correlation between these modules (**d**). Violin plots showing an increased expression of HSPR module in PD (**e**)

than in women, estrogen-based therapies have been investigated and, although the underlying mechanisms remain incompletely understood, they have shown neuroprotective effects in PD models [61, 67]. Notably, in a cuprizone-induced demyelination model, treatment with 17  $\beta$ -estradiol was found to prevent both demyelination and OL loss [73], supporting its potential to mitigate OL dysfunction in PD as well.

Collectively, these findings highlight the need to unravel the mechanisms underlying OLs dysfunction in PD, as such insights are crucial for guiding the development of therapies that protect myelin and promote neuronal health. Moreover, the role of PDA populations in exacerbating neurodegeneration through the disruption of essential glial–neuronal interactions underscores their critical contribution to the dysfunction of the basal ganglia circuit that characterizes PD.

## Conclusion

Our study provides a comprehensive characterization of oligodendroglia heterogeneity in the dorsal striatum of Parkinson's disease, highlighting distinct disease-associated subtypes with impaired myelination and immune-like properties. The emergence of these dysfunctional states suggests that OLs are not merely bystanders but active contributors to PD pathology. We hypothesize that a maladaptive oligodendroglia response—characterized by disrupted maturation, immune activation, and myelin instability—exacerbates neurodegeneration and impairs basal ganglia function. Targeting these pathogenic OLs states may offer novel therapeutic strategies to protect myelin integrity and slow disease progression.

**Supplementary Information** The online version contains supplementary material available at <https://doi.org/10.1007/s00401-025-02884-5>.

**Acknowledgements** The authors acknowledge the Massachusetts Alzheimer's Disease Research Center (especially Patrick Dooley and Tessa Connors), the Parkinson's UK Brain Bank at Imperial funded by Parkinson's UK (a charity registered in England and Wales, 258197, and in Scotland, SC037554), and the NIH NeuroBioBank (NIH Ref-1851, Requestor: Professor Ernest Arenas, R.I.P.), for the supply of tissue samples and associated clinical and neuropathological data. The authors also want to thank the National Genomics Infrastructure in Stockholm funded by Science for Life Laboratory and SNIC/Uppsala Multidisciplinary Center for Advanced Computational Science for assistance with massively parallel sequencing and access to the UPPMAX computational infrastructure. Further thanks go to Katarina Tiklova and Chika Yokota from the In Situ Sequencing Infrastructure Unit at the Science for Life Laboratory, Stockholm. The authors also thank Ayush Noori for making available his pathway clustering code which served as the foundation for our GSEA Superpathway analysis, and the *Centro de Investigación Biomédica en Red de Salud Mental-CIBERSAM* (CB/07/09/0033). Finally, we are extremely grateful to the brain donors and their families who have made this study possible.

**Author contributions** Concept and design: JMBR, ABMM Tissue acquisition and processing: LH, MJ, CMC, ASP, ABMM Sequencing: LH, ABMM Data analysis: JMBR, SMS, LDG, NR Interpretation of the data: JMBR, ABMM Supervision: ABMM Resources: MN, BTH, ASP, ABMM Writing—original draft: JMBR, ABMM Writing—review & editing: JMBR, LH, SMS, MN, BTH, ASP, ABMM.

**Funding** Funding for open access publishing: Universidad de Cádiz/CBUA. The authors acknowledge support from grants PID2019-109046GA-I00 and PID2022-136526OB-I00 by MCIN/AEI/<https://doi.org/10.13039/501100011033> and ERDF/EU (to A.B.M.-M. and 2019-FPI to J.M.B.-R.), RyC program RYC-2017-22594 (to A.B.M.-M.), the Swedish Foundation for Strategic Research FFL 18-0314 (A.B.M.-M.), the Swedish Research Council 2017-03349 (to A.B.M.-M.), the Prince Mahidol Award Youth Program (to M.J.), the Martin L. and Sylvia Seevak-Hoffman Fellowship for Alzheimer's Research (to M.J.), the Real Colegio Complutense at Harvard University (to C.M.-C.), and the US National Institute on Aging P30AG062421 (to B.T.H. and A.S.-P.).

**Availability of data and material** Single-nuclei RNA-seq and spatial transcriptomics data have been deposited at Figshare (10.6084/m9.figshare.28202405) and Zenodo (10.5281/zenodo.15304115) respectively and are publicly available as of the date of publication. Any additional information required to reanalyze the data reported in this paper is available from the lead contact upon request (Ana B. Muñoz-Manchado ([ana.munoz@uca.es](mailto:ana.munoz@uca.es))).

## Declarations

**Conflict of interest** Dr. Hyman owns stock in Novartis; he serves on the SAB of Dewpoint and has an option for stock. He serves on a scientific advisory board or is a consultant for AbbVie, Alexion, Ambagon, Aprinova Therapeutics, Arvinas, AvroBio, AstraZenica, Biogen, Bioinsights, BMS, Cure Alz Fund, Cell Signaling, Dewpoint, Latus, Merck, Novartis, Pfizer, Sanofi, Sofinova, Takeda, TD Cowen, Vigil, Violet, Voyager, WaveBreak. His laboratory is supported by research grants from the National Institutes of Health, Cure Alzheimer's Fund, Tau Consortium, and the JPB Foundation—and a sponsored research agreement from AbbVie and Sanofi. He has a collaborative project with Biogen. Dr. Marco Salas is co-founder of spatialist AB, a spatial omics consulting company.

**Ethical approval and consent to participate** The study does not include living human subjects. Samples were collected from autopsies and

have been de-identified. Donors or their next-of-kin provided written informed consent for brain autopsy, and the study was approved by the review board of each brain bank.

**Open Access** This article is licensed under a Creative Commons Attribution 4.0 International License, which permits use, sharing, adaptation, distribution and reproduction in any medium or format, as long as you give appropriate credit to the original author(s) and the source, provide a link to the Creative Commons licence, and indicate if changes were made. The images or other third party material in this article are included in the article's Creative Commons licence, unless indicated otherwise in a credit line to the material. If material is not included in the article's Creative Commons licence and your intended use is not permitted by statutory regulation or exceeds the permitted use, you will need to obtain permission directly from the copyright holder. To view a copy of this licence, visit <http://creativecommons.org/licenses/by/4.0/>.

## References

- Agarwal D, Sandor C, Volpato V, Caffrey TM, Monzón-Sandoval J, Bowden R et al (2020) A single-cell atlas of the human substantia nigra reveals cell-specific pathways associated with neurological disorders. *Nat Commun* 11:4183. <https://doi.org/10.1038/s41467-020-17876-0>
- Arai T, Uéda K, Ikeda K, Akiyama H, Haga C, Kondo H et al (1999) Argyrophilic glial inclusions in the midbrain of patients with Parkinson's disease and diffuse Lewy body disease are immunopositive for NACP/ $\alpha$ -synuclein. *Neurosci Lett* 259:83–86. [https://doi.org/10.1016/S0304-3940\(98\)00890-8](https://doi.org/10.1016/S0304-3940(98)00890-8)
- Bae E-J, Pérez-Acuña D, Rhee KH, Lee S-J (2023) Changes in oligodendroglial subpopulations in Parkinson's disease. *Mol Brain* 16:65. <https://doi.org/10.1186/s13041-023-01055-5>
- Bakiri Y, Káradóttir R, Cossell L, Attwell D (2011) Morphological and electrical properties of oligodendrocytes in the white matter of the corpus callosum and cerebellum. *J Physiol* 589:559–573. <https://doi.org/10.1113/jphysiol.2010.201376>
- Baumann N, Pham-Dinh D (2001) Biology of oligodendrocyte and myelin in the mammalian central nervous system. *Physiol Rev* 81:871–927. <https://doi.org/10.1152/physrev.2001.81.2.871>
- Bechler ME, Byrne L, French-Constant C (2015) CNS myelin sheath lengths are an intrinsic property of oligodendrocytes. *Curr Biol* 25:2411–2416. <https://doi.org/10.1016/j.cub.2015.07.056>
- Binamé F, Sakry D, Dimou L, Jolivel V, Trotter J (2013) NG2 regulates directional migration of oligodendrocyte precursor cells via Rho GTPases and polarity complex proteins. *J Neurosci* 33:10858–10874. <https://doi.org/10.1523/JNEUROSCI.5010-12.2013>
- Birk S, Bonafonte-Pardàs I, Feriz AM, Boxall A, Agirre E, Memi F et al (2025) Quantitative characterization of cell niches in spatially resolved omics data. *Nat Genet*. <https://doi.org/10.1038/s41588-025-02120-6>
- Blauwendraat C, Nalls MA, Singleton AB (2020) The genetic architecture of Parkinson's disease. *Lancet Neurol* 19:170–178. [https://doi.org/10.1016/S1474-4422\(19\)30287-X](https://doi.org/10.1016/S1474-4422(19)30287-X)
- Boshkovski T, Cohen-Adad J, Mistic B, Arnulf I, Corvol J-C, Vidailhet M et al (2022) The Myelin-weighted connectome in Parkinson's disease. *Mov Disord* 37:724–733. <https://doi.org/10.1002/mds.28891>
- Braak H, Tredici KD, Rüb U, de Vos RAI, Jansen Steur ENH, Braak E (2003) Staging of brain pathology related to sporadic Parkinson's disease. *Neurobiol Aging* 24:197–211. [https://doi.org/10.1016/S0197-4580\(02\)00065-9](https://doi.org/10.1016/S0197-4580(02)00065-9)
- Bradl M, Lassmann H (2010) Oligodendrocytes: biology and pathology. *Acta Neuropathol* 119:37–53. <https://doi.org/10.1007/s00401-009-0601-5>
- Bryois J, Skene NG, Hansen TF, Kogelman LJA, Watson HJ, Liu Z et al (2020) Genetic identification of cell types underlying brain complex traits yields insights into the etiology of Parkinson's disease. *Nat Genet* 52:482–493. <https://doi.org/10.1038/s41588-020-0610-9>
- Büttner M, Ostner J, Müller CL, Theis FJ, Schubert B (2021) scCODA is a Bayesian model for compositional single-cell data analysis. *Nat Commun* 12:6876. <https://doi.org/10.1038/s41467-021-27150-6>
- Chong SYC, Rosenberg SS, Fancy SPJ, Zhao C, Shen Y-AA, Hahn AT et al (2012) Neurite outgrowth inhibitor Nogo-A establishes spatial segregation and extent of oligodendrocyte myelination. *Proc Natl Acad Sci U S A* 109:1299–1304. <https://doi.org/10.1073/pnas.1113540109>
- Corces MR, Shcherbina A, Kundu S, Gloudemans MJ, Frésard L, Granja JM et al (2020) Single-cell epigenomic analyses implicate candidate causal variants at inherited risk loci for Alzheimer's and Parkinson's diseases. *Nat Genet* 52:1158–1168. <https://doi.org/10.1038/s41588-020-00721-x>
- Dean DC, Hurley SA, Kecskemeti SR, O'Grady JP, Canda C, Davenport-Sis NJ et al (2017) Association of amyloid pathology with myelin alteration in preclinical Alzheimer disease. *JAMA Neurol* 74:41–49. <https://doi.org/10.1001/jamaneuro.2016.3232>
- Dehestani M, Kozareva V, Blauwendraat C, Fraenkel E, Gasser T, Bansal V (2024) Transcriptomic changes in oligodendrocytes and precursor cells associate with clinical outcomes of Parkinson's disease. *Mol Brain* 17:56. <https://doi.org/10.1186/s13041-024-01128-z>
- Depp C, Sun T, Sasmita AO, Spieth L, Berghoff SA, Nazarenko T et al (2023) Myelin dysfunction drives amyloid- $\beta$  deposition in models of Alzheimer's disease. *Nature* 618:349–357. <https://doi.org/10.1038/s41586-023-06120-6>
- DeTomaso D, Yosef N (2021) Hotspot identifies informative gene modules across modalities of single-cell genomics. *Cell Syst* 12:446–456.e9. <https://doi.org/10.1016/j.cels.2021.04.005>
- Dickson DW, Braak H, Duda JE, Duyckaerts C, Gasser T, Halliday GM et al (2009) Neuropathological assessment of Parkinson's disease: refining the diagnostic criteria. *Lancet Neurol* 8:1150–1157. [https://doi.org/10.1016/S1474-4422\(09\)70238-8](https://doi.org/10.1016/S1474-4422(09)70238-8)
- Domingues HS, Portugal CC, Socodato R, Relvas JB (2016) Oligodendrocyte, astrocyte, and microglia crosstalk in myelin development, damage, and repair. *Front Cell Dev Biol* 4:71. <https://doi.org/10.3389/fcell.2016.00071>
- Errea O, Rodríguez-Oroz MC (2021) Oligodendrocytes, a new player in the etiology of Parkinson's disease. *Mov Disord* 36:83. <https://doi.org/10.1002/mds.28393>
- Falcão AM, van Bruggen D, Marques S, Meijer M, Jäkel S, Agirre E et al (2018) Disease-specific oligodendrocyte lineage cells arise in multiple sclerosis. *Nat Med* 24:1837–1844. <https://doi.org/10.1038/s41591-018-0236-y>
- Fan L-Y, Yang J, Liu R-Y, Kong Y, Guo G-Y, Xu Y-M (2023) Integrating single-nucleus sequence profiling to reveal the transcriptional dynamics of Alzheimer's disease, Parkinson's disease, and multiple sclerosis. *J Transl Med* 21:649. <https://doi.org/10.1186/s12967-023-04516-6>
- de Faria O, Dhaunchak AS, Kamen Y, Roth AD, Kuhlmann T, Colman DR et al (2019) TMEM10 promotes oligodendrocyte differentiation and is expressed by oligodendrocytes in human remyelinating multiple sclerosis plaques. *Sci Rep* 9:3606. <https://doi.org/10.1038/s41598-019-40342-x>
- Franklin RJM (2002) Why does remyelination fail in multiple sclerosis? *Nat Rev Neurosci* 3:705–714. <https://doi.org/10.1038/nrn917>

28. Garma LD, Harder L, Barba-Reyes JM, Marco Salas S, Díez-Salguero M, Nilsson M et al (2024) Interneuron diversity in the human dorsal striatum. *Nat Commun* 15:6164. <https://doi.org/10.1038/s41467-024-50414-w>
29. Glass CK, Saijo K, Winner B, Marchetto MC, Gage FH (2010) Mechanisms underlying inflammation in neurodegeneration. *Cell* 140:918–934. <https://doi.org/10.1016/j.cell.2010.02.016>
30. Goldenberg MM (2012) Multiple sclerosis review. *PT* 37:175–184
31. Halliday GM, Holton JL, Revesz T, Dickson DW (2011) Neuro-pathology underlying clinical variability in patients with synucleinopathies. *Acta Neuropathol* 122:187–204. <https://doi.org/10.1007/s00401-011-0852-9>
32. Hawrylycz MJ, Lein ES, Guillozet-Bongaarts AL, Shen EH, Ng L, Miller JA et al (2012) An anatomically comprehensive atlas of the adult human brain transcriptome. *Nature* 489:391–399. <https://doi.org/10.1038/nature11405>
33. Herz DM, Eickhoff SB, Løkkegaard A, Siebner HR (2014) Functional neuroimaging of motor control in Parkinson's disease: a meta-analysis. *Hum Brain Mapp* 35:3227–3237. <https://doi.org/10.1002/hbm.22397>
34. del Horteaga PR (1928) Tercera aportación al conocimiento morfológico e interpretación funcional de la oligodendroglía [Third contribution to the morphological knowledge and functional interpretation of oligodendroglia]. *Memorias de la Real Soc Española de Historia Nat* 14:5–122
35. Jäkel S, Agirre E, Falcão AM, van Bruggen D, Lee KW, Knuesel I et al (2019) Altered human oligodendrocyte heterogeneity in multiple sclerosis. *Nature* 566:543–547. <https://doi.org/10.1038/s41586-019-0903-2>
36. Jia F, Fellner A, Kumar KR (2022) Monogenic Parkinson's disease: genotype, phenotype, pathophysiology, and genetic testing. *Genes (Basel)* 13:471. <https://doi.org/10.3390/genes13030471>
37. Jin S, Guerrero-Juarez CF, Zhang L, Chang I, Ramos R, Kuan C-H et al (2021) Inference and analysis of cell-cell communication using Cell Chat. *Nat Commun* 12:1088. <https://doi.org/10.1038/s41467-021-21246-9>
38. Kalafatakis I, Karageorgos D (2021) Oligodendrocytes and microglia: key players in myelin development. *Damage Repair Biomol* 11:1058. <https://doi.org/10.3390/biom11071058>
39. Kang M, Yao Y (2022) Laminin regulates oligodendrocyte development and myelination. *Glia* 70:414–429. <https://doi.org/10.1002/glia.24117>
40. Kirby BB, Takada N, Latimer AJ, Shin J, Carney TJ, Kelsh RN et al (2006) In vivo time-lapse imaging shows dynamic oligodendrocyte progenitor behavior during zebrafish development. *Nat Neurosci* 9:1506–1511. <https://doi.org/10.1038/nn1803>
41. Kish SJ, Shannak K, Hornykiewicz O (1988) Uneven pattern of dopamine loss in the striatum of patients with idiopathic Parkinson's disease. *N Engl J Med* 318:876–880. <https://doi.org/10.1056/NEJM198804073181402>
42. Kleshchevnikov V, Shmatko A, Dann E, Aivazidis A, King HW, Li T et al (2022) Cell 2location maps fine-grained cell types in spatial transcriptomics. *Nat Biotechnol* 40:661–671. <https://doi.org/10.1038/s41587-021-01139-4>
43. Korsunsky I, Millard N, Fan J, Slowikowski K, Zhang F, Wei K et al (2019) Fast, sensitive and accurate integration of single-cell data with harmony. *Nat Methods* 16:1289–1296. <https://doi.org/10.1038/s41592-019-0619-0>
44. Labouesse MA, Torres-Herraez A, Chohan MO, Villarin JM, Greenwald J, Sun X et al (2023) A non-canonical striatopallidal Go pathway that supports motor control. *Nat Commun* 14:6712. <https://doi.org/10.1038/s41467-023-42288-1>
45. Marco Salas S, Kuemmerle LB, Mattsson-Langseth C, Tismeyer S, Avenel C, Hu T et al (2025) Optimizing Xenium in situ data utility by quality assessment and best-practice analysis workflows. *Nat Methods* 22:813–823. <https://doi.org/10.1038/s41592-025-02617-2>
46. Marques S, Zeisel A, Codeluppi S, van Bruggen D, Mendanha Falcão A, Xiao L et al (2016) Oligodendrocyte heterogeneity in the mouse juvenile and adult central nervous system. *Science* 352:1326–1329. <https://doi.org/10.1126/science.aaf6463>
47. Mathys H, Davila-Velderrain J, Peng Z, Gao F, Mohammadi S, Young JZ et al (2019) Single-cell transcriptomic analysis of Alzheimer's disease. *Nature* 570:332–337. <https://doi.org/10.1038/s41586-019-1195-2>
48. Mathys H, Peng Z, Boix CA, Victor MB, Leary N, Babu S et al (2023) Single-cell atlas reveals correlates of high cognitive function, dementia, and resilience to Alzheimer's disease pathology. *Cell* 186:4365–4385.e27. <https://doi.org/10.1016/j.cell.2023.08.039>
49. Miguel-Hidalgo JJ (2022) Astroglia in the vulnerability to and maintenance of stress-mediated neuropathology and depression. *Front Cell Neurosci*. <https://doi.org/10.3389/fncel.2022.869779>
50. Miguel-Hidalgo JJ (2023) Neuroprotective astroglial response to neural damage and its relevance to affective disorders. *Explor Neuroprotective Ther*. 3:328–345. <https://doi.org/10.37349/ent.2023.00054>
51. Nasrabad SE, Rizvi B, Goldman JE, Brickman AM (2018) White matter changes in Alzheimer's disease: a focus on myelin and oligodendrocytes. *Acta Neuropathol Commun* 6:22. <https://doi.org/10.1186/s40478-018-0515-3>
52. Ouchi Y, Yoshikawa E, Sekine Y, Futatsubashi M, Kanno T, Ogusu T et al (2005) Microglial activation and dopamine terminal loss in early Parkinson's disease. *Ann Neurol* 57:168–175. <https://doi.org/10.1002/ana.20338>
53. Palla G, Spitzer H, Klein M, Fischer D, Schaar AC, Kuemmerle LB et al (2022) Squidpy: a scalable framework for spatial omics analysis. *Nat Methods* 19:171–178. <https://doi.org/10.1038/s41592-021-01358-2>
54. Pandey S, Shen K, Lee S-H, Shen Y-AA, Wang Y, Otero-García M et al (2022) Disease-associated oligodendrocyte responses across neurodegenerative diseases. *Cell Rep* 40:111189. <https://doi.org/10.1016/j.celrep.2022.111189>
55. Poewe W, Seppi K, Tanner CM, Halliday GM, Brundin P, Volkmann J et al (2017) Parkinson disease. *Nat Rev Dis Primers* 3:17013. <https://doi.org/10.1038/nrdp.2017.13>
56. Politis M (2014) Neuroimaging in Parkinson disease: from research setting to clinical practice. *Nat Rev Neurol* 10:708–722. <https://doi.org/10.1038/nrneuro.2014.205>
57. Pringsheim T, Jette N, Frolkis A, Steeves TDL (2014) The prevalence of Parkinson's disease: a systematic review and meta-analysis. *Mov Disord* 29:1583–1590. <https://doi.org/10.1002/mds.25945>
58. Rajan S, Sood A, Jain R, Kamatham PT, Khatri DK (2024) Fingolimod exerts neuroprotection by regulating S1PR1 mediated BNIP3-PINK1-Parkin dependent mitophagy in rotenone induced mouse model of Parkinson's disease. *Neurosci Lett* 820:137596. <https://doi.org/10.1016/j.neulet.2023.137596>
59. Reyes JF, Rey NL, Bousset L, Melki R, Brundin P, Angot E (2014) Alpha-synuclein transfers from neurons to oligodendrocytes. *Glia* 62:387–398. <https://doi.org/10.1002/glia.22611>
60. Ruppert MC, Greuel A, Tahmasian M, Schwartz F, Stürmer S, Maier F et al (2020) Network degeneration in Parkinson's disease: multimodal imaging of nigro-striato-cortical dysfunction. *Brain* 143:944–959. <https://doi.org/10.1093/brain/awaa019>
61. Rymbai E, Sugumar D, Chakkittukandiyil A, Kothandan R, Selvaraj D (2024) Molecular insights into the potential effects of selective estrogen receptor  $\beta$  agonists in Alzheimer's and Parkinson's diseases. *Cell Biochem Funct* 42:e4014. <https://doi.org/10.1002/cbf.4014>

62. Sadick JS, O'Dea MR, Hasel P, Dykstra T, Faustin A, Liddelov SA (2022) Astrocytes and oligodendrocytes undergo subtype-specific transcriptional changes in Alzheimer's disease. *Neuron* 110:1788–1805.e10. <https://doi.org/10.1016/j.neuron.2022.03.008>
63. Sharma S, Mathur AG, Pradhan S, Singh DB, Gupta S (2011) Fingolimod (FTY720): first approved oral therapy for multiple sclerosis. *J Pharmacol Pharmacother* 2:49–51. <https://doi.org/10.4103/0976-500X.77118>
64. Smajčić S, Prada-Medina CA, Landoulsi Z, Ghelfi J, Delcambre S, Dietrich C et al (2022) Single-cell sequencing of human midbrain reveals glial activation and a Parkinson-specific neuronal state. *Brain* 145:964–978. <https://doi.org/10.1093/brain/awab446>
65. Snaidero N, Möbius W, Czopka T, Hekking LHP, Mathisen C, Verkleij D et al (2014) Myelin membrane wrapping of CNS axons by PI(3,4,5)P3-dependent polarized growth at the inner tongue. *Cell* 156:277–290. <https://doi.org/10.1016/j.cell.2013.11.044>
66. Son S-J, Kim M, Park H (2016) Imaging analysis of Parkinson's disease patients using SPECT and tractography. *Sci Rep* 6:38070. <https://doi.org/10.1038/srep38070>
67. Song Y, Li S, Li X, Chen X, Wei Z, Liu Q et al (2020) The effect of estrogen replacement therapy on Alzheimer's disease and Parkinson's disease in postmenopausal women: a meta-analysis. *Front Neurosci*. <https://doi.org/10.3389/fnins.2020.00157>
68. Stassen SV, Kobashi M, Lam EY, Huang Y, Ho JWK, Tsia KK (2024) StaVia: spatially and temporally aware cartography with higher-order random walks for cell atlases. *Genome Biol* 25:224. <https://doi.org/10.1186/s13059-024-03347-y>
69. Street K, Rizzo D, Fletcher RB, Das D, Ngai J, Yosef N et al (2018) Slingshot: cell lineage and pseudotime inference for single-cell transcriptomics. *BMC Genomics* 19:477. <https://doi.org/10.1186/s12864-018-4772-0>
70. Sun Y, Ji J, Zha Z, Zhao H, Xue B, Jin L et al (2021) Effect and mechanism of catalpol on remyelination via regulation of the NOTCH1 signaling pathway. *Front Pharmacol* 12:628209. <https://doi.org/10.3389/fphar.2021.628209>
71. Surmeier DJ, Graves SM, Shen W (2014) Dopaminergic modulation of striatal networks in health and Parkinson's disease. *Curr Opin Neurobiol* 29:109–117. <https://doi.org/10.1016/j.conb.2014.07.008>
72. Takagi S, Hayakawa N, Kimoto H, Kato H, Araki T (2007) Damage to oligodendrocytes in the striatum after MPTP neurotoxicity in mice. *J Neural Transm (Vienna)* 114:1553–1557. <https://doi.org/10.1007/s00702-007-0790-9>
73. Taylor LC, Puranam K, Gilmore W, Ting JP-Y, Matsushima GK (2010) 17  $\beta$ -estradiol protects male mice from cuprizone-induced demyelination and oligodendrocyte loss. *Neurobiol Dis* 39:127–137. <https://doi.org/10.1016/j.nbd.2010.03.016>
74. Teeple E, Joshi P, Pande R, Huang Y, Karambe A, Latta-Mahieu M et al (2021) Single nuclei sequencing of human putamen oligodendrocytes reveals altered heterogeneity and disease-associated changes in Parkinson's disease and multiple system atrophy. *BioRxiv*. <https://doi.org/10.1101/2021.05.06.442967>
75. Thomason EJ, Escalante M, Osterhout DJ, Fuss B (2020) The oligodendrocyte growth cone and its actin cytoskeleton: a fundamental element for progenitor cell migration and CNS myelination. *Glia* 68:1329–1346. <https://doi.org/10.1002/glia.23735>
76. Törner R, Kupreichyk T, Hoyer W, Boisbouvier J (2022) The role of heat shock proteins in preventing amyloid toxicity. *Front Mol Biosci*. <https://doi.org/10.3389/fmolb.2022.1045616>
77. Tsai H-H, Niu J, Munji R, Davalos D, Chang J, Zhang H et al (2016) Oligodendrocyte precursors migrate along vasculature in the developing nervous system. *Science* 351:379–384. <https://doi.org/10.1126/science.aad3839>
78. Virtanen P, Gommers R, Oliphant TE, Haberland M, Reddy T, Cournapeau D et al (2020) SciPy 1.0: fundamental algorithms for scientific computing in Python. *Nat Methods* 17:261–272. <https://doi.org/10.1038/s41592-019-0686-2>
79. Wakabayashi K, Hayashi S, Yoshimoto M, Kudo H, Takahashi H (2000) NACP/ $\alpha$ -synuclein-positive filamentous inclusions in astrocytes and oligodendrocytes of Parkinson's disease brains. *Acta Neuropathol* 99:14–20. <https://doi.org/10.1007/PL00007400>
80. Wang L-Y, Yu X, Li X-X, Zhao Y-N, Wang C-Y, Wang Z-Y et al (2019) Catalpol exerts a neuroprotective effect in the MPTP mouse model of Parkinson's disease. *Front Aging Neurosci* 11:316. <https://doi.org/10.3389/fnagi.2019.00316>
81. Wang Q, Song L-J, Ding Z-B, Chai Z, Yu J-Z, Xiao B-G et al (2022) Advantages of Rho-associated kinases and their inhibitor fasudil for the treatment of neurodegenerative diseases. *Neural Regen Res* 17:2623–2631. <https://doi.org/10.4103/1673-5374.335827>
82. Wolf FA, Angerer P, Theis FJ (2018) SCANPY: large-scale single-cell gene expression data analysis. *Genome Biol* 19:15. <https://doi.org/10.1186/s13059-017-1382-0>
83. Wolff AW, Bidner H, Remane Y, Zimmer J, Aarsland D, Rascol O et al (2024) Protocol for a randomized, placebo-controlled, double-blind phase IIa study of the safety, tolerability, and symptomatic efficacy of the ROCK-inhibitor Fasudil in patients with Parkinson's disease (ROCK-PD). *Front Aging Neurosci*. <https://doi.org/10.3389/fnagi.2024.1308577>
84. Wolock SL, Lopez R, Klein AM (2019) Scrublet: computational identification of cell doubles in single-cell transcriptomic data. *Cell Syst* 8:281–291.e9. <https://doi.org/10.1016/j.cels.2018.11.005>
85. Xu J, Farsad HL, Hou Y, Barclay K, Lopez BA, Yamada S et al (2023) Human striatal glia differentially contribute to AD- and PD-specific neurodegeneration. *Nat Aging* 3:346–365. <https://doi.org/10.1038/s43587-023-00363-8>
86. Xu X, Han Y, Zhang B, Ren Q, Ma J, Liu S (2024) Understanding immune microenvironment alterations in the brain to improve the diagnosis and treatment of diverse brain diseases. *Cell Commun Signal* 22:132. <https://doi.org/10.1186/s12964-024-01509-w>
87. Yang K, Wu Z, Long J, Li W, Wang X, Hu N et al (2023) White matter changes in Parkinson's disease. *npj Parkinsons Dis*. 9:1–10. <https://doi.org/10.1038/s41531-023-00592-z>
88. Zeisel A, Muñoz-Manchado AB, Codeluppi S, Lönnerberg P, La Manno G, Juréus A et al (2015) Cell types in the mouse cortex and hippocampus revealed by single-cell RNA-seq. *Science* 347:1138–1142. <https://doi.org/10.1126/science.aaa1934>
89. Zhao P, Yang X, Yang L, Li M, Wood K, Liu Q et al (2017) Neuroprotective effects of fingolimod in mouse models of Parkinson's disease. *FASEB J* 31:172–179. <https://doi.org/10.1096/fj.20160751R>

**Publisher's Note** Springer Nature remains neutral with regard to jurisdictional claims in published maps and institutional affiliations.